Stably-Inverted Apical-Out Human Upper Airway Organoids for SARS-CoV-2 Infection and Therapeutic Testing

Ji-Hoon Lee[1,2+], Julia C. LeCher[3,4+], Eric Parigoris[1,2], Noriyuki Shinagawa[1], Jason Sentosa[1], Candela Manfredi[4,5], Shu Ling Goh[3,4], Ramyani De[3,4], Sijia Tao[3,4], Keivan Zandi[3,4], Franck Amblard[3,4], Eric J. Sorscher[4,5], Jason R. Spence[6,7], Rabindra Tirouvanziam[1,5,8], Raymond F. Schinazi[3*], Shuichi Takayama[1,2*]

[1]Wallace H. Coulter Department of Biomedical Engineering, Georgia Institute of Technology and Emory University School of Medicine, Atlanta, GA, USA

[2]The Parker H. Petit Institute of Bioengineering and Bioscience, Georgia Institute of Technology, Atlanta, GA USA

[3]Center for Viroscience and Cure, Laboratory of Biochemical Pharmacology, Department of Pediatrics, Emory University School of Medicine and Children's Healthcare of Atlanta, Atlanta, GA, USA

[4]Department of Pediatrics, Emory University School of Medicine, Atlanta, GA, USA

[5]Children's Healthcare of Atlanta, Atlanta, GA, USA

[6]Division of Gastroenterology, Department of Internal Medicine, Department of Cell and Developmental Biology, University of Michigan Medical School, Ann Arbor, MI, USA

[7]Department of Biomedical Engineering, University of Michigan College of Engineering, Ann Arbor, MI, USA

[8]Center for CF and Airways Disease Research, Children's Healthcare of Atlanta, Atlanta, GA, USA

+These two authors contributed equally to this work

*E-mails: rschina@emory.edu, takayama@gatech.edu

Keywords:

Organoid, apical-out, SARS-CoV-2, antiviral testing, remdesivir, AT-511, nirmatrelvir, standardization, basal cells

Abstract

Apical-out organoids produced through eversion triggered by extra-organoid extracellular matrix (ECM) removal or degradation are generally small, structurally variable, and limited for viral infection and therapeutics testing. This work describes ECM-encapsulating, stably-inverted apical-out human upper airway organoids (AORBs) that are large (~500 µm diameter), consistently spherical, recapitulate *in vivo*-like cellular heterogeneity, and maintain their inverted morphology for over 60 days. Treatment of AORBs with IL-13 skews differentiation towards goblet cells and the apical-out geometry allows extra-organoid mucus collection. AORB maturation for 14 days induces strong co-expression of ACE2 and TMPRSS2 to allow high-yield infection with five SARS-CoV-2 variants. Dose-response analysis of three well-studied SARS-CoV-2 antiviral compounds [remdesivir, bemnifosbuvir (AT-511), and nirmatrelvir] shows AORB antiviral assays to be comparable to gold-standard air-liquid interface cultures, but with higher throughput (~10-fold) and fewer cells (~100-fold). While this work focuses on SARS-CoV-2 applications, the consistent AORB shape and size, and one-organoid-per-well modularity broadly impacts *in vitro* human cell model standardization efforts in line with economic imperatives and recently updated FDA regulation on therapeutic testing.

Main text

Introduction

Organoids recapitulate physiological tissue functions and reflect human biological variability, such as responsiveness to different therapeutics[1], and, thus, play a critical role in the drug development pipeline. The functional features of organoids arise from stem or progenitor cell differentiation and assembly within a basement membrane protein-rich extracellular matrix (ECM) milieu. Organoid design typically includes a large excess of ECM, resulting in undesirable variability in cellular self-organization and leading to organoids of various shapes, sizes, and numbers. In lung organoid virus infection studies, the excess ECM surrounding the organoids and their generally apical-in structure limit the access of viruses and therapeutics to apically expressed receptors (**Extended Data Fig. 1**)[2–5]. Thus, despite their proven physiological tissue functionality, these limitations can hinder the scalability, standardization, and broader use of lung organoids in studies of the normal and diseased human airway and therapeutic development.

This paper describes a bioengineering solution to these challenges based on organoid self-organization in minimal ECM to produce stably-inverted apical-out human upper airway organoids in a one-organoid, one-well format (**Fig. 1a**). Unlike well-established conventional cultures, where macroscopic ECM domes surround the organoid exterior (**Fig. 1b**)[6], our method results in cells surrounding a minimal amount of Matrigel scaffolding compartmentalized in the organoid interior[7–10]. While apical-out lung organoids can be produced from conventional cultures through the removal of extra-organoid ECM to trigger eversion[11,12], the structures are small, often incompletely everted and appear inherently less stable, perhaps due to the removal of ECM. Importantly, direct organoid viral infection rates reported in the literature are inconsistent, or even omitted[13]. This limitation stems from a fundamental challenge in conventional Matrigel dome culture: difficulty in controlling the number of organoids within each well and ensuring consistent viral delivery to the apical surface (**Extended Data Fig. 1**). As a result, accurately quantifying viral infection rates becomes a challenging task. In contrast, our ECM-encapsulating inverted organoids are produced in a one-organoid, one-per-well manner using an eversion-free mechanism (**Extended Data Fig. 2**), and have a basal-in, stably apical-out structure that successfully remains structurally sustainable for over 60 days (**Extended Data Fig. 4**). In addition, our organoids can be scaled up to 384-well plate for use in high-throughput screening (HTS) platforms. For brevity, we refer to these 3D cellular constructs as "airway organoids with reversed biopolarity" (AORBs).

AORBs consist of physiologically relevant, *in vivo*-like, differentiated human upper respiratory epithelium and are readily infected with high yield (>95%) by five severe acute respiratory syndrome coronavirus 2 (SARS-CoV-2) variants. The stably apical-out design allows direct access of the virus to the apical face, while absence of extra-organoid ECM gel facilitates virus transport as well as exposure to antiviral compounds. Each AORB contains sufficient cells for single-organoid downstream qRT-PCR analysis of virus infection. During evaluation of the antiviral activity of three anti-SARS-CoV-2 drugs, two of which are Food and Drug Administration (FDA)-approved and one in a phase III trial[14], the antiviral efficacy results of AORBs corroborates those of the gold-standard transwell 24-well air-liquid interface (ALI) cultures, but with significantly higher throughput in the 384-well format.

The field of everted- and inverted-organoids is a growing sub-field within the general organoid arena. Despite using similar starting cells, media, and supplements, the different material manipulations not only result in an inside-out geometry but also often lead to altered cellular differentiation. The demonstrated differentiation into all major bronchial epithelial cell types, stable inversion, and expression of the appropriate receptors and co-receptors for SARS-CoV-2 infection on the exterior, marks a significant advance in the manufacture of functional inverted upper airway organoids. Matrigel encapsulation by the epithelial cells stimulates the cellular production of a native basement membrane on the organoid interior, enhancing inversion stability. This ECM-filled structure also allows for large-diameter organoids without a necrotic core, as most cells are on the surface, ensuring proper nutrient and oxygen diffusion. These features underscore the bioengineering significance of this work, enabling HTS in a one-organoid-per-well format (**Fig. 1a and Extended Data Fig. 2c**) for studies of the human airway and therapeutic development.

Results

Cell-assisted minimal Matrigel scaffolding supports high-throughput, robust, and single-organoid-per-well culture of AORBs.

We previously described eversion-free methods for generating geometrically-inverted mammary organoids[7,8,10]. Additionally, we successfully adapted the methods for culturing kidney proximal tubule organoids, stably maintaining their inverted structure for over 100 days[9]. A key material manipulation method is to 'prematurely' gel minimal Matrigel using warm media to culture the cells with sufficient, but not excessive, growth factors to promote cell assembly and epithelial sheet formation[8]. AORB production builds upon these general principles but was applied here to human bronchial/tracheal epithelial cells (hBTECs) cultured in 384-array hanging drop (HD) plates[15] (**Extended Data Fig. 2**). Unique considerations for the use of hBTECs included identifying appropriate media conditions for initial AORB formation, as well as subsequent cellular differentiation. Unlike conventional apical-in organoids with a basement membrane that surrounds the organoid exterior (**Fig. 1b**), AORBs not only compartmentalize Matrigel in their core but also produce their own basement membrane on the interior surface (**Figs. 1c-e**). Optimization experiments culminated in a standard operating procedure (SOP) for AORB formation and culture (**Extended Data Fig. 2**).

The optimized SOP uses 3,000 cells per 25 μL droplet, Matrigel (50-107 μg/ml), fetal bovine serum (FBS) (<2%), and methylcellulose (0.24%) in a base medium. We achieved high-throughput (up to 384/plate) and robust AORB culture in a one-AORB-per-well format (**Extended Data Fig. 2**). AORBs remained stable for at least 60 days (**Extended Data Fig. 4**) with the diameter and roundness plateauing at consistent values (**Fig. 1f**). The compositions of the AORB seeding/formation and differentiation media are summarized in **Supplementary Table 1**. Analysis of >1,000 AORBs shows straightforward diameter modulation by adjusting Matrigel concentration (**Fig. 1g**) and the number of cells seeded (**Fig. 1h**). This observation held true across five donors (**Fig. 1i and Extended Data Figs. 5a-e; Table 1**) and across batches (**Extended Data Fig. 5f**), supporting the robustness of our SOP.

AORBs comprise physiologically-relevant differentiated airway cell types

Geometrical inversion was evidenced by exterior localization of apical markers acetylated α-tubulin (α-tub) on ciliated cells (**Fig. 2a and Extended Data Figs. 6a-e**) and mucin-5AC (MUC5AC) from goblet cells (**Fig. 2b**). In addition, live cell imaging confirmed beating apical-faced cilia (**Supplementary Videos 1-4**). Integrin beta-4 (ITGβ4) (**Fig. 2b**) and integrin alpha 6 (ITGα6) (**Fig. 2c**) were localized towards the interior of AORBs, confirming the inverted polarity. Images at lower magnification showed the stable global distribution of markers throughout AORBs (**Extended Data Figs. 6a-c and 7a-e**). We note that it is not uncommon for differentiated organoids to lose their basal progenitor cell population[16,17], as they differentiate into different subtype airway cells (**Extended Data Figs. 8b**). In AORBs, however, keratin 5 (KRT5) staining showed sustained presence of correctly oriented basal cells together with the differentiated cells, reminiscent of physiological cell heterogeneity and tissue structure (**Fig. 2c**).

Bulk RNAseq differential gene expression (DGE) analysis comparing AORB to their 2D undifferentiated counterparts revealed 7521 upregulated genes and 7100 downregulated genes (**Fig. 2d and Extended Data Fig. 8a**; **Supplementary Data 1**). AORBs showed downregulation

145 of basal cell markers (**Extended Data Fig. 8b**), and upregulation of ciliated cell markers
146 (**Extended Data Fig. 8c**). However, statistical tests suggested that the canonical markers of goblet
147 cells (*MUC5AC*, *MUC5B*) were not differentially expressed in AORBs (**Extended Data Fig. 8d**);
148 notably however, membrane-tethered mucins (*MUC1*, *MUC4*, *MUC16*) were upregulated
149 (**Extended Data Fig. 8d**). Also notably, there was an upregulation of gene signatures of ionocytes
150 (**Extended Data Fig. 8e**), a rare and understudied cell type of the respiratory epithelium with
151 unique expression of the cystic fibrosis transmembrane conductance regulator protein[18,19], further
152 suggesting physiological relevance of our AORBs.

153 Gene ontology (GO) analysis was performed to assess enriched biological processes
154 (**Fig. 2e**; **Supplementary Data 2**). Upregulated processes included cell-cell adhesions, ECM
155 organization, GTPase mediated signaling, and epithelial tube morphogenesis. Downregulated
156 processes included rRNA processing, rRNA metabolism, and ribosome biogenesis, implying a
157 differentiated state of AORBs[20]. The reduced proliferative state of AORBs was confirmed with
158 negative log2FoldChange (LFC) of *MKI67*, *PCNA*, *MCM2*, and *CDK1* (**Extended Data Fig. 8f**).
159 ECM organization-associated genes were also upregulated (**Supplemental Information**). Overall,
160 DGE analysis implied the maturation and differentiation of AORBs. Results from signaling
161 pathway impact analysis (SPIA) further substantiate that pathways for focal adhesion and ECM-
162 receptor interaction are activated, whereas cell cycle and protein processing in the endoplasmic
163 reticulum are inhibited (**Supplementary Data 3**).

164 scRNAseq of AORBs identified clusters of physiologically-relevant cell types (**Figure 2f**).
165 Representative canonical markers of ciliated (**Figures 2g-h**), basal (**Figures 2i-j**), and goblet cells
166 (**Figures 2k-l**) were all enriched in the corresponding clusters. Reference-based mapping of the
167 results based on the Human Lung Cell Atlas (HLCA)[21] also showed relevant markers of cell types
168 in these clusters (**Extended Data Figs. 8g-n**). Collectively, these data validated conversion of
169 cultures from dividing basal epithelial progenitors to a fully differentiated, physiologically relevant
170 representation of the upper human airway. Furthermore, the proportions of ciliated, basal, and
171 goblet cells were approximately 20% for each. These proportions are consistent with those
172 observed *in vivo*[22], albeit slightly lower.

173 **IL-13 induces increased apical-out mucus hypersecretion**

174 Interleukin-13 (IL-13) is a cytokine whose role in goblet cell metaplasia and mucus
175 hypersecretion has been extensively studied[23–25]. To explore the functional aspect of the apical-out
176 mucus secretion, AORBs were treated with 1 ng/mL IL-13 for 72 h (**Fig. 3a)** and mucins observed
177 via bright field microscopy (**Fig. 3b**) and fluorescent lectin assays (**Fig. 3c and Extended Data**
178 **Fig. 9**). Time-lapse imaging captured beating cilia clearing mucus on the apical surface
179 (**Supplementary Videos 3-4**). In contrast, untreated AORBs showed qualitatively less mucus
180 (**Fig. 3d**), suggesting stimulation of mucus hypersecretion by IL-13 (**Fig. 3e**). DGE analysis of IL-
181 13-treated AORBs vs. untreated AORBs (**Supplementary Data 4)** confirmed upregulation of
182 positive regulators of mucus secretion (*ANO1*, *ADORA3*, *ALOX12B*) and previously reported IL-
183 13-induced mucus metaplasia related genes[26] (*SPDEF*, *FOXA3*, *MUC2*, *MUC6*, *MUC5AC*,
184 *CLCA1*, *ALOX15B*), and downregulation of negative regulators of mucus secretion (*ADA*) and
185 ciliated cell markers (*TUBA1A*, *FOXJ1*) (**Fig. 3f**).

186 **AORBs express SARS-CoV-2 entry-associated genes.**

187 It is well established that SARS-CoV-2 uses angiotensin-converting enzyme 2 (ACE2) and
188 serine protease transmembrane serine protease 2 (TMPRSS2) for host cell entry.
189 Immunofluorescent imaging confirmed expression of ACE2 and TMPRSS2 on the apical surface
190 of AORBs (**Fig. 4a** and **Extended Data Figs. 7f-g**). Complementary scRNAseq analysis
191 confirmed expression of *ACE2* and *TMPRSS2* genes (**Figs. 4c-d**). ACE2 and TMPRRS2
192 expression steadily increased over 14 days, followed by a plateau (**Fig. 4b and Extended Data**
193 **Fig. 7**). Moreover, TMPRSS2 had a diffuse pattern of staining (**Fig. 5b**), while ACE2 was
194 restricted (**Fig. 5c**), in agreement with previous observations that while TMPRSS2 is expressed
195 throughout the membrane of airway epithelial cells (**Extended Data Figs. 7f-g**), ACE2 is restricted
196 to the apical face of primarily ciliated and goblet cells, with some expression on club and basal
197 cells[27–32]. DGE analysis (**Supplementary Data 1**) confirmed the statistically significant
198 upregulation of *ACE2* and *TMPRRS2*, as well as that of other membrane proteases and toll-like
199 receptors implicated in SARS-CoV-2 infection and epithelial cell responses (**Fig. 4e**).

200 **SARS-CoV-2 efficiently infects AORBs with >95% yield.**

201 Utilizing an infectious SARS-CoV-2-mNeon Green expressing clone (icSARS-CoV-2-
202 mNG)[33], we demonstrated replication of icSARS-CoV-2-mNG in AORBs (**Figs. 5a-f**), with the
203 reporter detectable throughout the AORBs (**Fig. 5a)** and co-localized to cells co-expressing ACE2
204 and TMPRSS2 (**Fig. 5f**) at 72 hpi. Orthogonal projections taken at the depth of the nucleus showed
205 intracellular expression of the mNG reporter (**Fig. 5f**), further validating SARS-CoV-2 infectibility.
206 As expected, because ACE2 and TMPRSS2 expression is higher, the more mature Day-14 AORBs
207 showed higher infectibility than Day-7 AORBs (**Fig. 5g**). RNAseq analysis confirmed expression
208 of all SARS-CoV-2 genes in infected AORBs (**Extended Data Fig. 10a**). Viral yields were ~0.5
209 log lower in AORBs compared with 2D and Transwell ALI cultures (**Extended Data Fig. 10b**).
210 This finding is particularly impressive considering the lower initial virus amounts used to maintain
211 a constant MOI. It is worthwhile noting that organoids formed from sub-optimal media conditions
212 (**Extended Data Fig. 10c)** failed to support productive virus replication (**Extended Data Fig. 10b**),
213 indicating the critical importance of the optimized SOP. An optimized infection of 72 h at MOI
214 1.0 resulted in high levels of infection (>95% of AORBs) and was used for subsequent assays.

215 We confirmed that not only the ancestral SARS-CoV-2 Lineage A Washington strain, but
216 also variants Alpha, Gamma, Delta, and Omicron, all productively infected AORBs (**Fig. 5h**). At
217 3 dpi, SARS-CoV-2 genome copies were within the same order of magnitude for Washington,
218 Alpha, and Gamma, while the genome copies for Delta and Omicron were 1–2 orders of magnitude
219 higher with respect to the others, consistent with previous observations[34]. There was no significant
220 difference in replication between donors for both Delta and Omicron (**Extended Data Fig. 10d**).

221 **RNAseq reveals differing epithelial responses to Washington, Delta, and Omicron.**

222 The top 10 upregulated biological processes found by GO analysis performed on AORBs
223 infected with SARS-CoV-2 Washington strain vs. uninfected negative controls included ribosome
224 processing, translation, and respiration (**Figs. 6a-b**). This was in direct contrast to the
225 downregulated processes for AORBs with respect to 2D basal cells (**Extended Data Fig. 8b**).
226 SPIA identified three relevant activated pathways involving COVID-19, NF-κB and TNF
227 signaling (**Fig. 6a, b**; **Supplementary Data 5**). Further analyses of subsets of relevant host
228 epithelial defense response genes for Washington, Delta, and Omicron showed similar

229 transcriptional changes upon infection with Washington and Omicron strains, and some difference
230 in Delta compared to the other two (**Fig. 6c**). More specifically, Washington and Omicron strains
231 showed similar patterns of transcriptional changes in type I interferon (IFN) (*ISG15*, *IRF3*, *IRF7*),
232 cytokine (*TNF*, *IL1B, CXCL8*, *MMP1*, *MMP3*), NF-κB (*NFKB1, NFKBIA, RELA*), immune
233 mediator (*CD86*, *CEACAM5*), and apoptosis (*CASP3*, *CASP7*, *CYCS*, *FADD*, *APAF1*) genes, with
234 a few minor differences (*IRF7*, *IL6*) (**Figs. 6c**). The notable transcriptional differences observed
235 with the Delta strain included quantitative changes in overlapping genes for Washington and
236 Omicron with an increased extent of upregulation of other immune genes (*IFNL1*, *IFNG*, *IL12B*),
237 and downregulation of certain apoptosis genes (*CASP3*, *CASP7*, *CYCS*) (**Fig. 6c**).

238 **AORBs provide an efficient anti-SARS-CoV-2 compound HTS platform**

239 For SARS-CoV-2, nucleoside analogs (NAs) remdesivir[35] and molnupiravir[36], and 3C-like
240 protease inhibitor (PI), Paxlovid, are the only FDA-approved antiviral regimens to date. We tested
241 the antiviral potency of remdesivir, PF-07321332 (the PI component of Paxlovid; nirmatrelvir) as
242 well as of a guanine double NA prodrug currently in Phase 3 trial, AT-511[14]. Cell infection models
243 (AORBs, hBTEC-ALI, Calu-3, Caco-2, and Vero) were treated with 0-10 μM of compound and
244 infected with the Washington strain for 48 (Vero) or 72 h (AORBs, hBTEC-ALI, Calu-3, Caco-
245 2). Mean effective concentrations (EC_{50}) and EC_{90} values for all compounds were within range of
246 published values (**Table 2**)[37–42]. AT-511 applied against Washington strain in these 2D cell lines
247 has not been reported, but, in our hands exhibited limited activity. AT-511 is a double prodrug
248 requiring multiple cellular enzymes for processing into its active nucleoside 5'-triphosphate form
249 (NTP; AT-9010)[40]. We postulated that primary differentiated cultures might have an enhanced
250 ability for AT-511 → AT-9010 conversion over 2D cultures used in this study. To investigate this,
251 cells were treated with 10 μM of AT-511 for 4 hr, then the cellular fraction collected for analysis.
252 hBTEC cells had significantly higher NTP levels (170.8 ± 62.5 pmol/10^6 cells) compared with
253 Vero (0.89 ± 0.05 pmol/10^6 cells), Calu-3 (4.93 ± 0.06 pmol/10^6 cells), and Caco-2 (30.1 ± 2.4
254 pmol/10^6 cells), which could be related to its greater potency in hBTEC cells (**Supplementary**
255 **Table 2**).
256 Overall, $EC_{50/90}$ were lower in the ALI model compared with AORBs; however, these
257 differences were statistically insignificant. While AORB cultures had higher levels of variability
258 compared with ALI cultures, this was attributed to donor variability (**Supplementary Table 3**).
259 To investigate whether donor variability was an issue specific to AORBs, we generated matched
260 donor ALI and AORB cultures (donor 3) and performed concurrent dose response assays which
261 did not reveal any significant difference in obtained $EC_{50/90}$ values (data not shown).
262

Discussion

Historically, 3D cellular constructs with polarity reversal have been reported in human enteroids[43,44], airway spheroids[45,46], mammary acini[47,48], and kidney cysts[49,50]. Generally, such polarity inversion is pathological[47,48,51] and/or probabilistic[49,52,53]. Of these, it is important to recognize the early work by Pederson et al., where ion transport was demonstrated using apical-out nasal organoids, although the underlying mechanism of polarity inversion was not further studied[45,46]. Recent pioneering work from Amieva et al. developed the ECM removal methodology to reproducibly induce geometrical eversion of organoid polarity in a human enteroid model, producing apical-out morphology[54]. Additional studies have since adapted the ECM removal methodology, including cell-mediated ECM degradation, to other types of organoids[11,55–63]. Also, manipulation of the wnt/β-catenin and BMT signaling pathway has been proposed[64]. Such geometrically-inverted polarity has facilitated studies of host-pathogen interactions[11,12,55,59,60,62], ciliary dynamics[57], barrier integrity[54,61], nutrient uptake[54,58], bio-inspired robots[65], and more[56,63]. However, the ECM removal method of apical-out organoid cultures based on polarity eversion often results in undesirable instability and varying degrees of "apical-out-ness", both spatially and temporally. Such impractical results could be attributed to the poor and/or partial degree of the everted morphology. Moreover, because ECM removal methods rely on the conventional Matrigel embedding protocol, associated limitations, such as poor scalability, high variability, imaging/analysis challenges, and phenotype heterogeneity, remain unresolved[66].

The utility of AORBs was assayed as a platform for the study of SARS-CoV-2 and antiviral drug development. Robust expression of ACE2 (on the apical aspect) and TMPRSS2 in AORBs, as well as RNA-level expression of SARS-CoV-2 implicated entry factors, were confirmed. Unlike eversion organoids, AORBs were infected by SARS-CoV-2 in a high yield (>95% of all singular AORBs used). Efficient infection was attributed to the stable spatial and temporal apical-out characteristics of AORBs. Many organoid-like airway models for SARS-CoV-2 studies have been reported, often with contradictory results, and many reports fail to include information on infection yields, making it difficult to assess their practicality. Notably, in eversion distal lung organoids[11], SARS-CoV-2 yield is limited at <10%, and shows no viral tropism in ciliated cells, a primary target for SARS-CoV-2[67,68]. The AORB model, with the high infection rate and the one-per-well modularity with HTS capability, would provide a significant advantage in promoting standardization through robust and rigorous evaluation.

Immune evasion by SARS-CoV-2 is an area of active study. Overall, our data support the prevailing literature that the antiviral response to SARS-CoV-2 infection in upper airway tissues is attenuated[69]. Of the three strains probed in detail, Delta induced a more robust antiviral response and production of inflammatory cytokines, including increased ISGs and NF-kB pathway components. The profile of Omicron-induced genes more closely mirrored that seen with the Washington strain, with the notable exception of inflammatory cytokines IL1B, IL6 and CXCL8. These data are consistent with recent observations[70,71], though the difference in host antiviral responses to Washington versus other variants is still relatively understudied. We hope the exhaustive RNAseq dataset provided herein can expand upon and facilitate research endeavors. Collectively, our results suggest that AORBs could provide an efficient platform to study different viral mechanisms such as immune evasion, virulence, and transmissibility.

The $EC_{50/90}$ determined in this study for remdesivir, AT-511, and nirmatrelvir were similar to published values. Remdesivir potency in Vero cells ranged from 0.7 μM to over 20 μM[37–40,42,72],

307 while values in Calu-3 (0.01 μM – 2.4 μM) and Caco-2 (0.001 – 0.08 μM) cell lines are typically
308 lower[37,38]. This discrepancy could be explained by differing level of enzymes required to process
309 remdesivir to its active NTP form (e.g., carboxylesterase 1, CES1; and cathepsin A, CatA) in
310 different cell types. Such enzymes are expressed at high levels in the lung[73,74] and intestine[74,75],
311 which could underlie the improved activity of remdesivir in these cells. In ALI cultures, our EC_{50}
312 values were comparable to published observations[38,42], and not significantly different from those
313 obtained in AORBs. Regarding antiviral efficacy of AT-511 in hBTECs, Good et al. reported an
314 EC_{90} of 0.47 μM[41], similar to Atea's SUNRISE-3 clinical trial (~0.78 μM)[14,76]. Our values from
315 hBTEC-ALI and AORB cultures aligned with these reports. AT-511 had limited activity in 2D
316 cultures. Similar to our 2D results, Do et al. reported no activity of AT-511 against a Beta variant
317 strain in the Vero E6 clone and human hepatoma cells (Huh-7). However, in contrast to Good et
318 al., the ATEA clinical trial, and our data herein, Do et al. did not observe activity in hBTEC-ALI
319 cultures. They attributed this discrepancy to possible differences in metabolism of AT-511 to AT-
320 9010 in the different cell culture systems and/or differences in the experimental approach. Our
321 metabolism assay supports that 2D cell lines employed herein have a reduced capacity for
322 metabolism of AT-511 compared with hBTEC-ALI cultures. Values obtained for nirmatrelvir
323 were consistent with published observations of sub-micromolar activity in 2D and primary lung
324 cell lines[77].

325 With the FDA lifting the mandate for animal testing through the Modernization Act 2.0[78],
326 microphysiological systems are gaining recognition for their potential as predictive preclinical
327 models. In antiviral screening results (data not shown due to proprietary issues), AORBs
328 successfully detected false negatives (missed hits) and false positives (misidentified compounds)
329 when compared to 2D cell lines. This phenomenon was also seen with AT-511 and highlights the
330 critical role of 3D systems in drug discovery that are more predictive of candidate drug activity.
331 Additionally, AORBs successfully captured donor variability, as evidenced by the varying
332 replication potency and antiviral efficacy observed in AORBs derived from different donors.
333 Collectively, these findings suggest that AORBs could serve as a valuable *in-vivo*-like addition to
334 the repertoire of preclinical models for drug development and disease modeling.

335 In addition to the HTS and modularity benefits of AORBs, there are other noteworthy
336 advantages. Our method demonstrates high sustainability for two reasons. First, our minimal
337 Matrigel scaffolding technique utilizes ~2 orders of magnitude less ECM compared to the ECM-
338 embedding method. Second, just one P0 vial of cells can theoretically yield ~ 210,000 AORBs.
339 Moreover, culturing AORBs as free-floating entities in ALI HDs, openly exposed to air, suggests
340 that the ALI environment can have multiple impacts on AORBs. For instance, we can manipulate
341 the air composition to mimic various physiological or diseased conditions, providing valuable
342 insights into the underlying mechanisms of disease progression and facilitating drug development.

343 In conclusion, the lack of standardization in organoid production and characterization
344 poses a significant obstacle to fully harnessing their potential in advancing biological research and
345 clinical applications. We introduce AORBs as a promising approach towards standardization.
346 AORBs not only exhibit physiological relevance and high-yield virus infection through their
347 apical-out surface, but also enable standardized HTS approaches, owing to their consistent and
348 large size. With further research and development, AORBs hold promise for enhancing the
349 reproducibility, quality control, and scalability of organoid production for industrial applications,
350 as well as advancing our understanding of complex biological processes.

Methods

Chemistry

All compounds (remdesivir[79], AT-511[80], and nirmatrelvir[81]) were synthesized in-house by established protocols. Purity greater than 98% was confirmed by NMR and HPLC analysis.

2D immortalized cell line culture

For antiviral studies, the following immortalized/transformed cell lines were used: Caco-2 human colon epithelial cells (ATCC, HTB-37), Calu-3 human lung cancer cell line (ATCC, HTB-55), and Vero African Green Monkey kidney cells (ATCC, CCL-81). Media compositions were (1) Caco-2 and Calu-3: advanced Dulbecco's modified Eagle medium:F12 (DMEM:F12), 10% FBS, 100 U/mL penicillin-streptomycin (pen-strep) (Gibco, 15140122), and 2 µM L-glutamine (L-glut), (2) Vero: DMEM, 10% FBS, 100 U/mL pen-strep. For all experiments, cells were grown at 37°C in a 95% O_2, 5% CO_2 incubator.

2D primary human bronchial epithelial basal cell expansion

Primary normal human tracheal/bronchial epithelial cells, hTBECs, (Lonza, CC-2540S) were expanded in Pneumacult^{TM}-Ex Plus basal medium (STEMCELL Technologies, #05041) supplemented with Pneumacult^{TM}-Ex Plus 50X supplement (STEMCELL Technologies, #05042) and 0.5 mL of 200 mM hydrocortisone using the manufacturer's recommended seeding density of 3,500 cells/cm^2 on a T-75 cell culture flask (Corning). The cells were subcultured at the confluence of 70-80%. Upon collection, cells were passaged, used for organoid culture, or cryopreserved. Cells beyond passage number 4 were not used, as they did not yield adequate organoid formation.

Primary human bronchial Transwell air-liquid interface culture

For hBTEC-ALI cultures, 1.5x10^5 cells were seeded on a 24-well 0.4 µm polystyrene transwell insert (Corning® cat. #3470) coated with type 1 bovine collagen type IV (Advance BioMatrix, PureCol) in complete PneumaCult™-Ex Plus medium supplemented with hydrocortisone. After 3 days, media was removed from the upper apical chamber to expose this surface to the air and complete Pneuma-Cult™-ALI medium supplemented with Pneuma-Cult™-ALI supplements (STEMCELL™ Technologies, #05001), hydrocortisone, and heparin solution added to the basal chamber to induce differentiation. Media was refreshed in the basal compartment every 2-3 days for 4 weeks. Culture viability and establishment of an intact polarized epithelial layer was routinely analyzed by microscopic analysis of cell morphology, cilia beat frequency, mucus formation and the absence of barrier-leakage. For all experiments, cells were grown at 37 °C in a 95% O_2, 5% CO_2 incubator.

Preparation of hanging-drop plates

For at least one day prior to organoid seeding, a 384-well hanging-drop (HD) plate custom designed with injection molding (Xcentric) was soaked in 0.1% solution of Pluronic F108 (Sigma-Aldrich, 542342) in distilled water (diH_2O) (Gibco, 15230). On the day of organoid seeding, the HD plate was rinsed off with diH_2O and then air dried. The plate was then UV-sterilized (Analytik Jena, CL-1000) for 20 minutes on each side. While waiting, the wells of a sterile non-tissue-treated round-bottom 96-well plate (Corning, 351177) were each filled with 150 µl of diH_2O supplemented with 1% pen-strep. When the HD plate was fully sterilized, it was placed (sandwiched) between the bottom and the lid of the 96-well plate. The two troughs of the short-

392 edged sides were loaded with diH2O, which were then stuffed with sterile gauze pads. Lastly, the
393 long edges were each added with ~ 1 ml of diH_2O.

394 **Hanging-drop AORB culture**

395 The seeding solution was composed of Pneumacult™ Airway Organoid Basal Medium (Stemcell
396 Technologies, #05061) supplemented with the following additives: Pneumacult™ Airway
397 Organoid Seeding Supplement (Stemcell Technologies, #05062), methylcellulose (Sigma-Aldrich,
398 94378), and growth factor reduced Matrigel (Corning, 356231) (**Supplementary Table 1)**. First,
399 the seeding supplement was added to the base medium (10% concentration). Next, an appropriate
400 volume of methylcellulose was added (0.24% final concentration at the target volume)and the
401 solution warmed in a 37ºC bead bath (Fisher Scientific, GSGPD10). Once warm, Matrigel (at
402 5.35 μg/ml to 16.05 μg/ml final concentration) was then deliberately kept cold in ice and added to
403 the pre-warmed media. Next, the desired volume of cell suspension at a final concentration of
404 120,000 cells/ml (3000 cells per 25 μl of the droplet) was added. Throughout the process, it was
405 crucial to mix components very thoroughly. Immediately after the seeding solution was prepared,
406 an eight-channel repeater pipette (Eppendorf, 4861000120) was used to load the HD plate in a
407 staggered zigzag pattern (8 alternating rows x 24 columns = 192 wells). This pattern minimized
408 adjacent wells with droplets from merging.

409 **Maintenance of organoids**

410 The organoids were monitored as needed with a high-throughput imaging system (Thermo
411 Scientific, EVOS FL Auto 2). At days 3-4 of organoid seeding and every three days thereafter, the
412 media exchange procedure was performed using a liquid handler robot (Analytik Jena, CyBio
413 FeliX). Volumes to be removed from and added to the organoids were programmatically controlled
414 using the CyBio Composer software. The organoid differentiation medium (ODM) to be
415 exchanged with was Pneumacult™ Airway Organoid Basal Medium (Stemcell Technologies,
416 #05061) supplemented with Differentiation Supplements (Stemcell Technologies, #05063). It may
417 be necessary to pre-fill wells around the outer edges with an additional medium (typically no more
418 than ~5 μl) to prevent aspiration of organoids. Moreover, it is advised to limit the time of handling
419 HD plates outside the humidity-controlled incubator as much as possible to minimize evaporation
420 of the liquid drops. The HD plate was kept in a cell culture incubator (Thermo Scientific, VIOS
421 160i) with 5% CO_2 injection at 37ºC.

422 **Virus preparation**

423 The following reagents were deposited by the Centers for Disease Control and Prevention and
424 obtained through BEI Resources, NIAID, NIH: SARS-Related Coronavirus 2, Isolate hCoV-
425 19/USA-WA1/2020, NR-52281 (Washington strain) and Isolate USA/CA_CDC_5574/2020, NR-
426 54011 (Alpha), The following reagent was obtained through BEI Resources, NIAID, NIH: SARS-
427 Related Coronavirus 2, Isolate hCoV-19/USA/MD-HP01542/2021 (Lineage B.1.351), in Caco-3
428 cells, NR-55282, contributed by Andrew S. Pekosz. The following reagent was obtained through
429 BEI Resources, NIAID, NIH: SARS-Related Coronavirus 2, Isolate hCoV-19/Japan/TY7-
430 503/2021 (Brazil P.1), NR-54982, contributed by National Institute of Infectious Diseases. Delta
431 and Omicron strains were a kind gift from Dr. Mehul Suthar. icSARS-CoV-2-mNG was a kind
432 gift from Dr. Stefan Sarafianos. For Washington, icSARS-CoV-2-mNG, Alpha, Beta, and Gamma
433 strains, virus stocks were prepared in Vero CL81 cells, while stocks for Delta and Omicron strains
434 were prepared in Calu-3 cells. Virus titers were determined by ELIspot assay. In brief, Vero or

435 Calu-3 cells were infected with 10-fold serially diluted stock in 2% infection media (base media
436 with 2% FBS) for 90 minutes, after which inoculum was removed, and 2% methylcellulose
437 supplemented with 2% FBS was added. After 2 (Vero) or 3 (Calu-3) days, cells were fixed with a
438 1:1 ratio of ice-cold methanol:acetone for 30 minutes for removal from the BSL-3 facility. Wells
439 were blocked for 1 hour in Pierce™ clear milk blocking buffer (ThermoFisher, #37587), incubated
440 with primary antibody against spike protein diluted 1:5,000 in blocking buffer (Elabscience, E-
441 AB-V1006) overnight in a 37ºC incubator with 5% CO_2 injection, washed 3x with PBS, incubated
442 for 1 hr with secondary antibody (HRP-conjugated goat anti-rabbit; Invitrogen, 656120) at room
443 temperature, and washed 3x again then treated with 50 µl of True Blue™ peroxidase substrate
444 (SeraCare, 5510-0030) for detection of viral antigens. Plates were read on a CTL plate reader
445 (Immunospot®, ELISPOT reader). All virus infections were carried out in a BSL-3 level
446 laboratory at Emory University in accordance with the guidelines of the 6th edition of Biosafety
447 in Microbiological and Biomedical Laboratories and with the approval of the Emory University
448 Environmental Health and Safety Office.

449 **Antiviral Screening**

450 For standard 2D antiviral screening, cells (Caco-2, Calu-3, and Vero) were grown to confluency
451 ($1x10^5$ cells) in 96-well plates. Dose-response curves were performed by treating cells with 2-fold
452 serial dilutions (0 – 10 µM) of compounds of interest in respective base media containing 2% heat-
453 inactivated FBS (ΔFBS) then infected with SARS-CoV-2 at an MOI of 0.1 (Vero) or 1.0 (MOI of
454 0.01 as reported previously[37]) (Caco2, Calu-3) for 48 (Vero) or 72 hrs (Caco-2, Calu-3).
455 Cells/supernatants were collected in 150 µL RLT Buffer (Qiagen©) for downstream RNA
456 extraction (Qiagen©, RNeasy 96 extraction kit) and subsequent qRT-PCR to detect viral load. For
457 hBTEC-ALI, compounds were added at indicated dilutions to the basolateral chamber. Cells were
458 washed 3x with HEPES-buffered salt solution (HBSS) on the apical surface to remove excess
459 mucus, then infected by adding 50 µL of SARS-CoV-2 virus (MOI 1.0) to the apical chamber for
460 a 5 hr adsorption after which virus was removed and cells retained in ALI for an additional 3 days.
461 For AORB cultures, $3x10^3$ cells were seeded in hanging-drop suspension with Matrigel® Basement
462 Membrane Matrix (Corning, 356231) to generate a single organoid per well and cultured for 21+
463 days. AORBs cultured in the HD plate were first transferred to a 96-well ultra-low-attachment
464 plate (Corning, 7007). Each well in the plate contains a single AORB. To achieve this, a P200
465 pipette tip with its entry edge cut using a sterilized razor blade is utilized to ensure transfer without
466 shearing AORBs. Serially diluted compounds and virus (MOI 1.0) were added directly to the wells
467 for a period of 3 days. AORB-infected cultures were collected in 150 µL RLT Buffer (Qiagen©),
468 while hBTEC-ALI cultures were collected in 300 µL of Trizol™ Reagent and RNA extracted by
469 phenyl-chloroform method according to manufacturers' protocol (ThermoFisher Scientific). All
470 experiments were performed three independent times, each including technical duplicates or
471 triplicates.

472 **RNA extraction and RT-qPCR**

473 RNA was detected by real-time PCR using a 6-carboxyfluorescein (FAM)-labeled probe with
474 primers against SARS-CoV-2 non-structural protein 3 (nsp3). (SARS-CoV-2 FWD: AGA AGA
475 TTG GTT AGA TGA TGA TAG T; SARS-CoV-2 REV:TTC CAT CTC TAA TTG AGG TTG
476 AAC C; SARS-CoV-2 Probe: 56-FAM/TC CTC ACT GCC GTC TTG TTG ACC A/3BHQ_1)
477 RNA isolated from uninfected cells was used as a negative control for virus detection. RNA was
478 added to optimized 10 µM primer/probe mix in Mastermix (Quantabio, qScript™ XLT One-Step

479 RT-qPCR ToughMix®) and run on StepOne Plus real-time PCR (Roche) according to the
480 manufacturer's protocol. CT values were calculated from replicate groups, and virus yield was
481 then quantified via standard curve.

482 **Cellular Pharmacology Assays**

483 Cellular pharmacology assays were performed as previously described[36]. In brief, cells were plated
484 and treated with 10 µM AT-511 for 4 hrs. Vero, Calu-3, and Caco-2 were seeded at $1x10^6$ cells
485 per well in 12 well plates. hBTECs were grown at ALI with $1.5x10^5$ cells per transwell insert in
486 24-well plates. After 4 hr incubation with compound, cells were washed 2x with ice-cold PBS,
487 then scrapped to collect the cell pellets in 70% methanol. Extracted samples were subjected to
488 analysis by liquid chromatography mass spectrometry (LC-MS).

489 **AORBs cryosectioning**

490 AORBs (15-20 per tube) were first pooled from the HD plate with a cut P200 tip to prevent
491 shearing damage to AORBs. The medium was removed to the minimum extent possible. AORBs
492 were then washed three times with 1X PBS (Gibco, 10010), with 2-3 minutes between washes.
493 Next, AORBs were fixed in 4% PFA (Thermo Scientific, J61899-AP) in PBS for 30 minutes,
494 followed by PBS washing three times. At this point, the fixed AORBs can be stored at 4ºC or
495 processed further with embedding procedures. The first step was to incubate AORBs with 0.5%
496 methylene blue (RICCA, 4850-16) in PBS for ~10 minutes. Next, AORBs were carefully and
497 repeatedly washed until no blue stain bled out. AORBs were then transferred to optimal cutting
498 temperature (Tissue-Tek, OCT) compound (Sakura, 4583) in a cryomold (Polysciences, 18986-1),
499 with as little PBS as possible. The samples were flash-frozen by manipulating the cryomolds in
500 partially frozen molecular biology grade isopentane (Sigma-Aldrich, M32631). The frozen blocks
501 of samples may be kept at -80ºC for long-term storage. A cryostat (Thermo Scientific, CryoStar
502 NX70) at the histology core of the Parker H. Petit Institute for Bioengineering and Bioscience,
503 Georgia Tech, was used for cryosectioning. Sections of 10-20 mm thickness were collected, and
504 two to three sections were applied per glass slide. The slides were kept at -20ºC until further use
505 in hematoxylin and eosin (H&E) or immunofluorescence staining.

506 **Hematoxylin and Eosin staining and imaging**

507 H&E staining was performed using an autostainer system (Leica, ST5010). Briefly, slides with
508 AORB sections were first brought up to room temperature, and then stained by a pre-established
509 protocol. The stained slides were then coverslipped with Cytoseal 60 (Richard-Allan Scientific),
510 and imaged in color using a DMi8 microscope.

511 **Immunofluorescence staining of cryosections**

512 The slides were first brought to room temperature, and the boundary containing AORB sections
513 was highlighted with a hydrophobic pen (Electron Microscopy Sciences, #71310) to minimize
514 reagent use. This was followed by PBS washing X3, permeabilization with 0.2% Triton X-100
515 (Sigma-Aldrich, T8787) in PBS for 5 min, PBS washing X3, blocking with 4% BSA (Millipore
516 Sigma, #82-067) for 1 h at room temperature, and an overnight incubation with primary antibodies
517 at 4ºC. The following primary antibodies were prepared in 1% BSA in PBS at the specified
518 dilutions shown:

519 mouse anti-acetylated-α-tubulin (Santa Cruz Biotechnology, sc-23950; 1:50)

520 mouse anti-MUC5AC (Santa Cruz Biotechnology, sc-21701; 1:50)

521 rabbit anti-KRT5 (Abcam, ab53121; 1:1000)

522 rabbit anti-E-cad (Cell Signaling Technology, 3195S; 1:1600)

523 rat anti-ITGα6 (Santa Cruz Biotechnology, sc-19622; 1:50)

524 mouse Anti-ITGβ4 (ThermoFisher, MA5-17104; 1:100)

525 goat anti-ACE2 (R&D Systems, AF933; 1:500)

526 mouse anti-TMPRSS2 (Santa Cruz Biotechnology, sc-515727; 1:50)

527 rabbit anti-LAM5 (Abcam, ab14509; 1:200)

528 After overnight incubation, slides were washed 3x with 1% BSA solution, then incubated with
529 secondary antibody solution at room temperature for 2 h. Appropriate combinations of conjugated
530 secondary antibodies were used to match the host of the primary antibodies, and these included:

531 Alexa Fluor 488 donkey anti-goat (Invitrogen, A11055)

532 Alexa Fluor 488 donkey anti-rat (Invitrogen, A21208)

533 Alexa Fluor 568 anti-mouse (Invitrogen, A10037)

534 Alexa Fluor 647 anti-rabbit (Invitrogen, A31573)

535 **Immunofluorescence staining of whole-mount AORBs**

536 Whole-mount immunofluorescence staining of AORBs was adopted from previously established
537 protocol[81]. Briefly, fixed AORBs were permeabilized with 0.1% Tween (Sigma-Aldrich, P9416)
538 in PBS for 10 mins in 4ºC, washed 3x with PBS, incubated with a AORB washing buffer (BWB)
539 composed of 0.1% Triton X-100 and 0.2% BSA for 15 min in 4ºC, then incubated overnight with
540 primary antibody solution in BWB on a gentle rocker in 4ºC. After the overnight incubation period
541 with primary antibodies, AORBs were washed 3x with BWB with an incubation period of at least
542 20 mins between the three washing steps. The washed AORBs were then incubated with secondary
543 antibody solutions prepared in BWB and rocked overnight at 4ºC. Tubes from this step onward
544 should be wrapped with aluminum foil to prevent photobleaching. Upon finishing the incubation
545 with secondary antibodies, AORBs were washed 3x with PBS, then counterstained with DAPI for
546 ~30 min at room temperature on a rocker. Counterstained AORBs were finally washed with PBS
547 3 times, and transferred either into a chambered coverslip (ibidi, #80821) or onto a coverslip
548 depending on the magnification required.

549 **Whole-mount AORB confocal imaging**

550 The whole-mount staining protocol was adopted from previously established work[82]. Briefly, fixed
551 AORBs were first incubated with 0.1% TWEEN 20 (Sigma-Aldrich, P9416) in PBS at 4ºC for 10
552 minutes. AORBs were then washed with PBS 3 times, then incubated with organoid washing
553 buffer (OWB), composed of filtered (Millipore Sigma, SCGP00525) 0.1% Triton X-100 (Sigma-
554 Aldrich, T8787) and 0.2% BSA BSA (Millipore Sigma, #82-067) in PBS, at 4ºC for 15 minutes.
555 Primary and secondary antibody solutions were appropriately diluted in OWB. Both primary and
556 secondary antibody incubation steps involved overnight mixing at 4ºC on a rocker. AORBs were

557 then subsequently counterstained with DAPI, and samples were imaged on a Nikon W1 spinning
558 disk confocal microscope.

559 **AORB IL-13 treatment**

560 During the second media exchange routine, fresh medium with 1 ng/mL of IL-13 (Peprotech,
561 #200-13) was used to treat AORBs. Treatment conditions were controlled to test both negative
562 controls and IL-13 groups within the same plate. AORBs were imaged on EVOS to monitor
563 morphology and secretions daily.

564 **Fluorescent lectin assay**

565 Lectin with FITC conjugate (MilliporeSigma, L4895) was used for the fluorescence mucin binding
566 assay. Manufacturer recommended concentration of the reconstituted lectin was added. AORBs
567 pooled into a 12-well plate, then imaged under a DMi8 microscope. NucBlue (ThermoFisher,
568 R37605) was also used to track live cells along with lectin-bound mucin components.

569 **Bulk RNA sequencing**

570 For bulk RNA sequencing, about five organoids per condition were harvested from the HD plate
571 to DNase- and RNase-free tubes (Eppendorf, 022363344). In the case of 2D cells, adherent cells
572 were collected with a cell scraper (Sarstedt, 83.1380). The cells/organoids were lysed in RLT lysis
573 buffer (Qiagen, 79216) containing 1.0% β-mercaptoethanol (Sigma-Aldrich, M3148). The lysates
574 were transported in dry ice to Emory Integrated Genomics Core (EIGC), Emory University, where
575 further sample processing and sequencing were carried out. RNA was isolated using the Quick-
576 RNA Microprep Kit (Zymo Research). The cDNA was generated using the SMART-Seq® v4
577 Ultra® Low Input RNA Kit (Takara Bio). The final sequencing library was made using the Nextera
578 XT kit (Illumina). The library construction used Nextera XT chemistry, which tagmented 200 pg
579 of DNA and added adapters in one step. The fragmented and tagged DNA was then amplified for
580 12 cycles to incorporate dual-indexing sequencing adapters to generate the final library. A
581 combination of both concentration and library size patterning was used as QC metrics to determine
582 the success of the assay. UV Qubit fluorometer quantitation was used to determine the
583 concentration of the library. A Bio/Fragment Analyzer trace revealed the size distribution and
584 concentration of the final sequencing library. Based on these three parameters, we assigned library
585 scores to each library. Those with a passing score were then used for sequencing in NovaSeq
586 (Illumina). The read depth for the run was ~40 million reads/sample.

587 **Differential gene expression and functional analysis**

588 Demultiplexed raw FASTQ files provided by EIGC were downloaded to Georgia Tech's high-
589 performance computing cluster "Partnership for an Advanced Computing Environment (PACE)".
590 Quality control was first performed using FastQC[83]. Trimmomatic was then used to trim the raw
591 FASTQ files[84]. Upon passing quality requirements, the read fragments were aligned to the
592 reference human genome (GRCh38.p13) or SARS-CoV-2 genome (GENCODE) using the STAR
593 algorithm[85]. A custom Python script was written to generate a gene count matrix. Principal
594 component analysis was performed to sort out any outliers. Gene-level differential expression
595 analysis was conducted with DESeq2 package in R[86]. Briefly, raw reads were normalized by the
596 DESeq2's median of ratios method. Identified outliers and genes with low counts (mean counts <
597 2) were filtered out and not included for subsequent hypothesis testing. Lastly, computed LFC
598 values were shrunken with the ashr package to obtain more accurate estimates of LFC[87].

599 Differential expression testing was performed using the Wald test with Benjamin-Hochberg
600 multiple comparison correction. The cutoff for significance was set at an adjusted p-value <0.05
601 and LFC of ±0.6. Heatmaps and volcano plots were generated using the ggplot2 package.
602 GO/GSEA was conducted in clusterprofiler[88], and pathway analysis was performed by SPIA[89].

603 **scRNAseq**

604 scRNAseq of AORBs used the PIPseqTM pipeline (PIPseqTM T2 3' Single-Cell RNA kit v4.0,
605 Fluent BioSciences). The protocol was adapted from previous work[90]. Briefly, AORBs were
606 harvested onto a cell strainer (431750, Corning) to remove debris. The AORBs were washed and
607 pooled into a 1.5-mL Eppendorf tube, then dissociated into a single-cell suspension by incubating
608 in TrypLE (12604021, Gibco) at 37°C for 30 min with frequent mixing by pipetting. Subsequently,
609 cell viability was enhanced using a dead cell removal kit (130-090-101, Miltenyi Biotec). The
610 resulting purified cell suspension with improved viability (>95%) was diluted according to the
611 manufacturer's recommendation (1250 cells/µL). PIPSeq kits were applied to capture mRNA,
612 synthesize cDNA, and construct libraries. Libraries that passed QC were then used for sequencing
613 on a 100-cycle NovaSeq SP kit, with read lengths as specified by the user guide. FASTQ files were
614 first preprocessed with the same QC and trimming tools as described above. Subsequent
615 computational analysis of the raw data was performed using PIPseeker v3.0 Software. RNA data
616 processing steps included mapping with STAR aligner, transcript counting, cell calling, clustering,
617 and differential expression. UMAPs and feature plots were generated as the final outputs.

618 **Statistical Analysis**

619 GraphPad Prism 10.0.2 was used to perform statistical analyses. Median effective concentration
620 of compounds (EC_{50}) and concentrations with a 90% inhibitory effect (EC_{90}) of the three
621 compounds tested were calculated and reported as the mean ± standard deviation. One-way
622 ANOVA and subsequent Tukey's post-hoc tests were used to compare the means of AORB
623 diameters at differing Matrigel levels, donors, and batches. An alpha of 0.05 was used as a
624 threshold for statistical significance.

Data Availability

The main data supporting the results in this study are available within the paper and its Supplementary Information. The raw and analyzed datasets are available for research purposes from the corresponding author upon reasonable request. Our RNAseq data have been deposited on Gene Expression Omnibus (GEO) of NCBI and are available under the SuperSeries accession number GSE249581.

Acknowledgements

This research was supported by NIH (R01-HL-136141; R01-AI-161570; R01-HL-139876), NSF EBICS (CBET 0939511), Price Gilbert Jr Chair's Fund, Biomedical Engineering Department Seed funds, and the Center for AIDS Research at Emory University (P30-AI-050409). The study was also supported in part by the Emory Integrated Genomics Core (EIGC), which is subsidized by the Emory University School of Medicine and is one of the Emory Integrated Core Facilities. Furthermore, this work was supported in part through research cyberinfrastructure resources and services provided by the Partnership for an Advanced Computing Environment (PACE) at the Georgia Institute of Technology, Atlanta, Georgia, USA. We also wish to acknowledge the core facilities at the Parker H. Petit Institute for Bioengineering and Bioscience at the Georgia Institute of Technology for the use of their shared equipment, services, and expertise. We thank Dr. Greg Gibson and the Atlanta Single-cell Omics and Analytics Institute (AScOmAI) for assistance with scRNAseq. We also would like to thank Drs. Mehul Suthar and Stefan Sarafianos of Emory University for their kind donation of SARS-CoV-2 variants.

Author Contributions

Conceptualization: JHL, EP, RFS, ST; Formal analysis: JHL, JCL, NS, JS; Funding acquisition: RFS, ST; Investigation: JHL, JCL; Methodology: JHL, JCL, CM, SLG, RD, RFS, ST; Project administration: JHL, JCL; Experimental approach: JHL, JCL, KZ, FA, EJS, JRS, RT, RFS, ST; Supervision: ST, RFS; Writing manuscript: JHL, JCL, ST; Manuscript review & editing: all authors.

JHL and JCL contributed equally to this work.

Competing Interests

The authors declare no competing interest.

Additional Information

Extended data is available for this paper at ~

Supplementary information is available for this paper at ~

Correspondence and requests for materials should be addressed to Raymond F. Schinazi and Shuichi Takayama

Figures and Tables

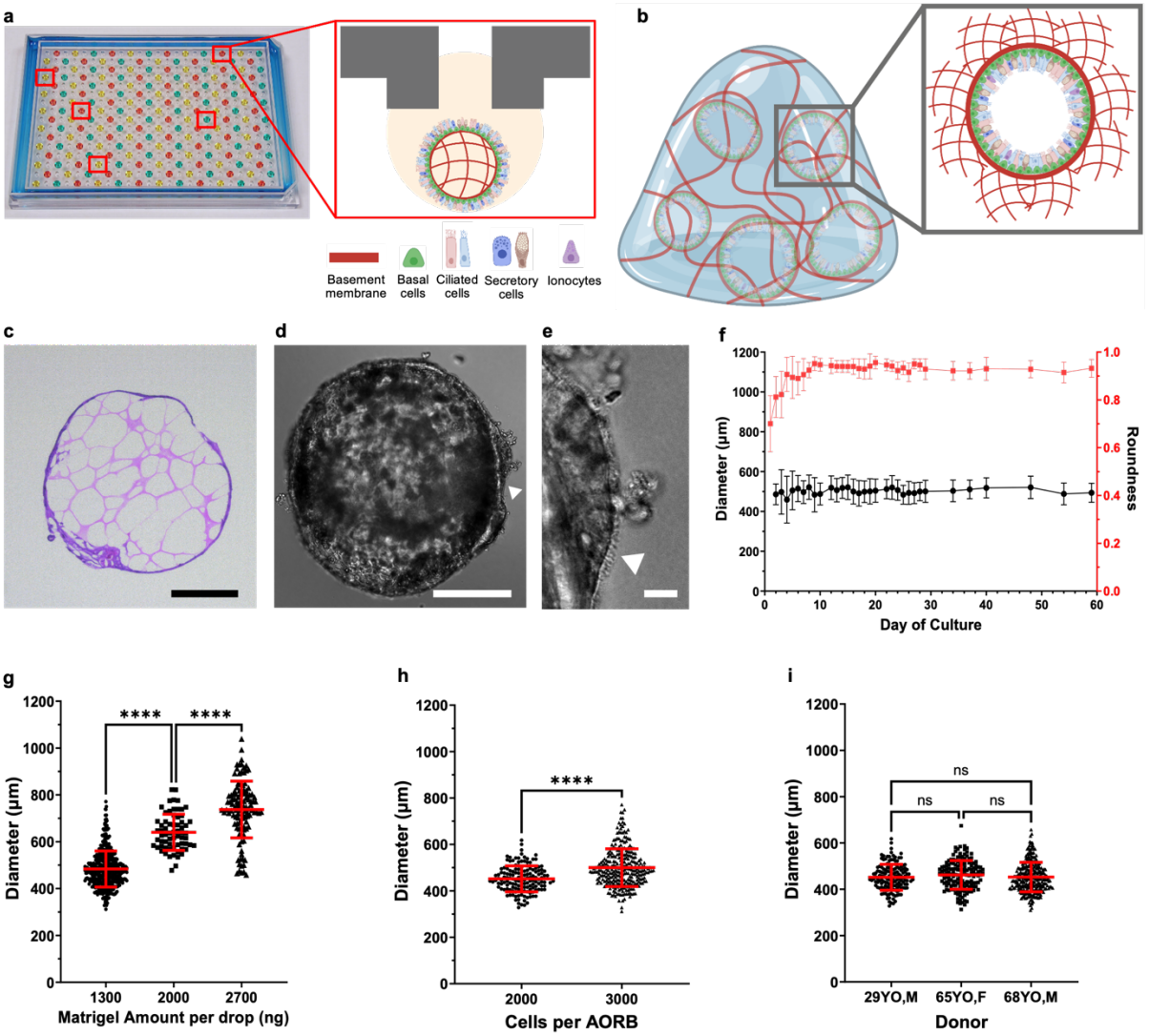

Fig. 1| **Human upper airway epithelial organoid with reversed biopolarity (AORBs)**. **a**, A 192 hanging drop array culture of single AORB-per-drop provides throughput and consistency. Eversion-free stably-inverted AORBs have terminally differentiated and physiologically relevant cell types. **b**, Conventional Matrigel-dome method of organoid culture has an exterior basement membrane with the apical side facing the interior. **c**, H&E staining shows an epithelial layer shell with a core filled with Matrigel. **d**, Phase-contrast image of an entire AORB, and **e**, a zoomed-in image showing cilia (denoted by triangles) and AORB-produced mucus. **f**, The diameters of AORBs are stable over 80 days, whereas the roundness increases up to day 10 of culture then stabilizes. **g**, For a given number of starting cells, Matrigel amount can alter AORB diameters. **h**, Seeding density also provides a statistically significant means of regulating AORB diameters. **i**, For a given Matrigel amount and cell density, AORB diameters are consistent across biological donors. ns, $p>0.05$, ****$p<0.0001$. Scale bars, 250 µm in **c** and **d**, and 20 µm in **e**.

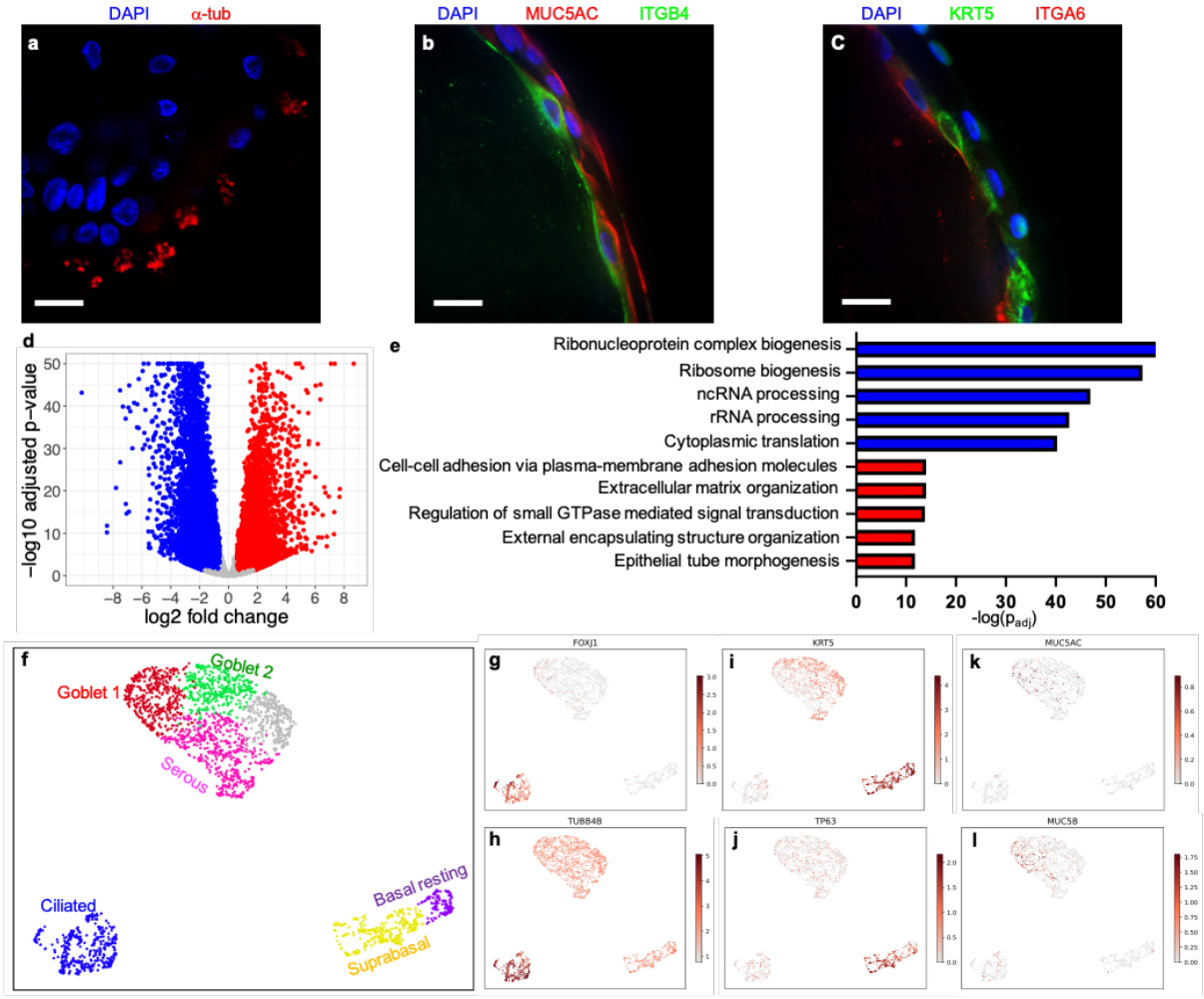

Fig. 2| **Confocal Immunofluorescence imaging confirms heterogeneous cell population and apical-out polarization in AORBs**. **a**, Acetylated alpha tubulin orienting outwards indicating that the apical side of the ciliated cells face the organoid exterior. **b**, AORBs also have positive MUC5AC (red) indicative of goblet cells. ITGB4 (green) binds the basement membrane and indicates the basolateral side is facing the organoid interior. **c**, KRT5 (green) and ITGA6 (red) stains indicate the presence of basal cells. **d**, Volcano plot from bulk RNA sequencing comparing transcriptomic profile of the differentiated AORBs with respect to the initial cells before seeding (2D cultures) shows 7521 upregulated and 7100 downregulated genes. **e**, Top 5 statistically significant upregulated (red) and downregulated (blue) biological processes from gene ontology analysis of the enriched gene sets from DGE analysis. **f**, UMAP of scRNAseq results (n=2651 cells) of AORBs showing three main clusters, ciliated, basal, and secretory. Further clustering shows sub-cell types, reprehensive of human bronchi. **g-l**, Canonical markers of ciliated cells (**g** and **h**), basal cells (**i** and **j**), and goblet cells (**k** and **l**). Color bars represent log-transformed normalized expression. Scale bars, 20 µm, in **a-c**.

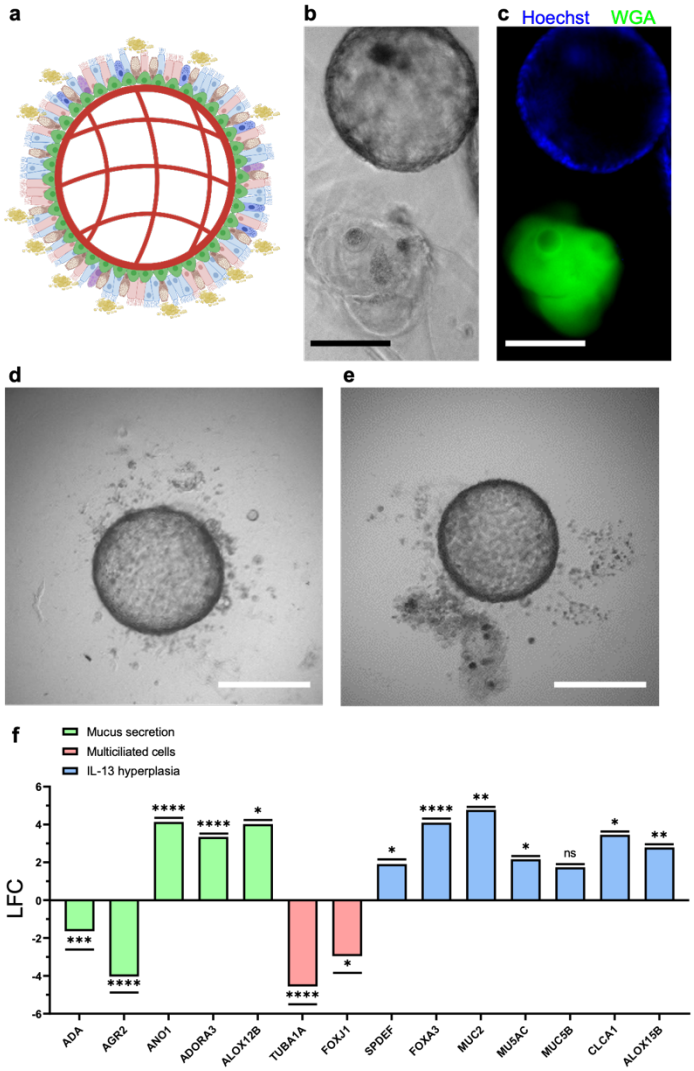

Fig. 3| **IL-13-induced apical-out mucus hypersecretion experiment. a,** Apical-out morphology in AORBs allows efficient assay to study mucus secretion. **b** and **c**, Bright-field and immunofluorescent images of an AORB treated with 1 ng/mL IL-13, respectively. Nuclei and mucus are stained with Hoechst 33342 (blue) and wheat germ agglutinin (green). **d**, Representative bright-field images of untreated AORBs. **e**, Representative bright-field images of IL-13-treated. **f**, DGE analysis results (IL-13-treated vs. untreated) for genes associated with mucus secretion, multiciliated cells, and IL-13 hyperplasia. Scale bars, 500 μm in **b**-**e**.

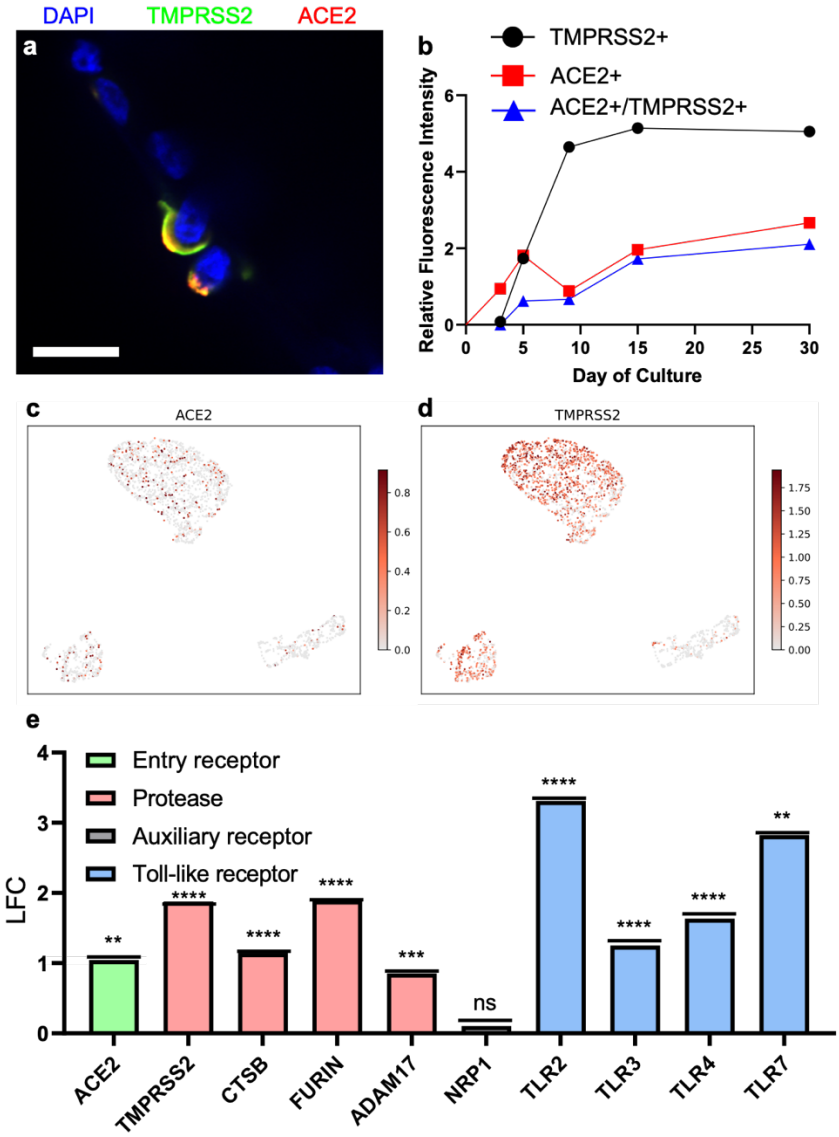

Fig. 4| **AORBs robustly express SARS-CoV-2-implicated entry factors. a,** Immunofluorescence imaging confirms apical-out expression of ACE2 (red) and TMPRSS2 (green). **b**, Semi-quantitative analysis results show a time-dependent increase in levels of fluorescence for ACE2+, TMPRSS2+, and ACE2+/TMPRSS2+ cells. **c**, scRNAseq *ACE2* expression. **d**, scRNAseq *TMPRSS2* expression. scRNAseq reveals higher *TMPRSS2* expression levels than *ACE2*. DGE analysis reveals upregulation of many other SARS-CoV-2 entry factors in AORBs with respect to 2D monolayer culture. Scale bar, 20 µm in **a**.

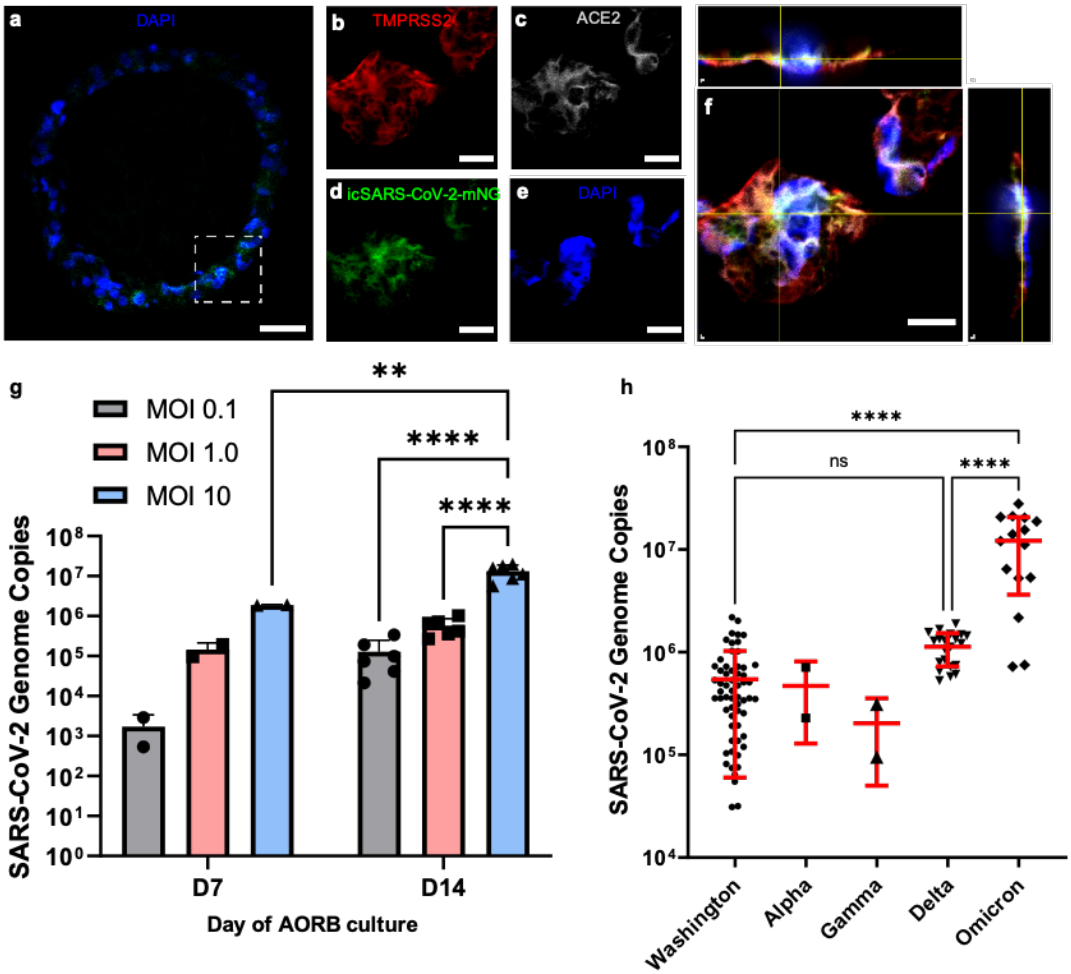

Fig. 5| **AORBs are infected by SARS-CoV-2. a**, Section of a AORB overlay stained for nuclei (blue, DAPI) and replicated SARS-CoV-2 (green, icSARS-CoV-2-mNG). **b-f**, Zoomed in immunofluorescence images of stains for TMPRSS2, replicated viruses, ACE2, nuclei, and an overlay and orthogonal projections of these four markers, respectively. **g**, Increasing the MOI results in expected increases in replication. More mature AORBs show higher infectibility consistent with their higher expression of ACE2/TMRPRSS2 levels (see Fig 4b). **h**, AORB infection results with 5 different SARS-CoV-2 variants. Scale bars, 100 µm in **a**, and 10 µm in **b-f**.

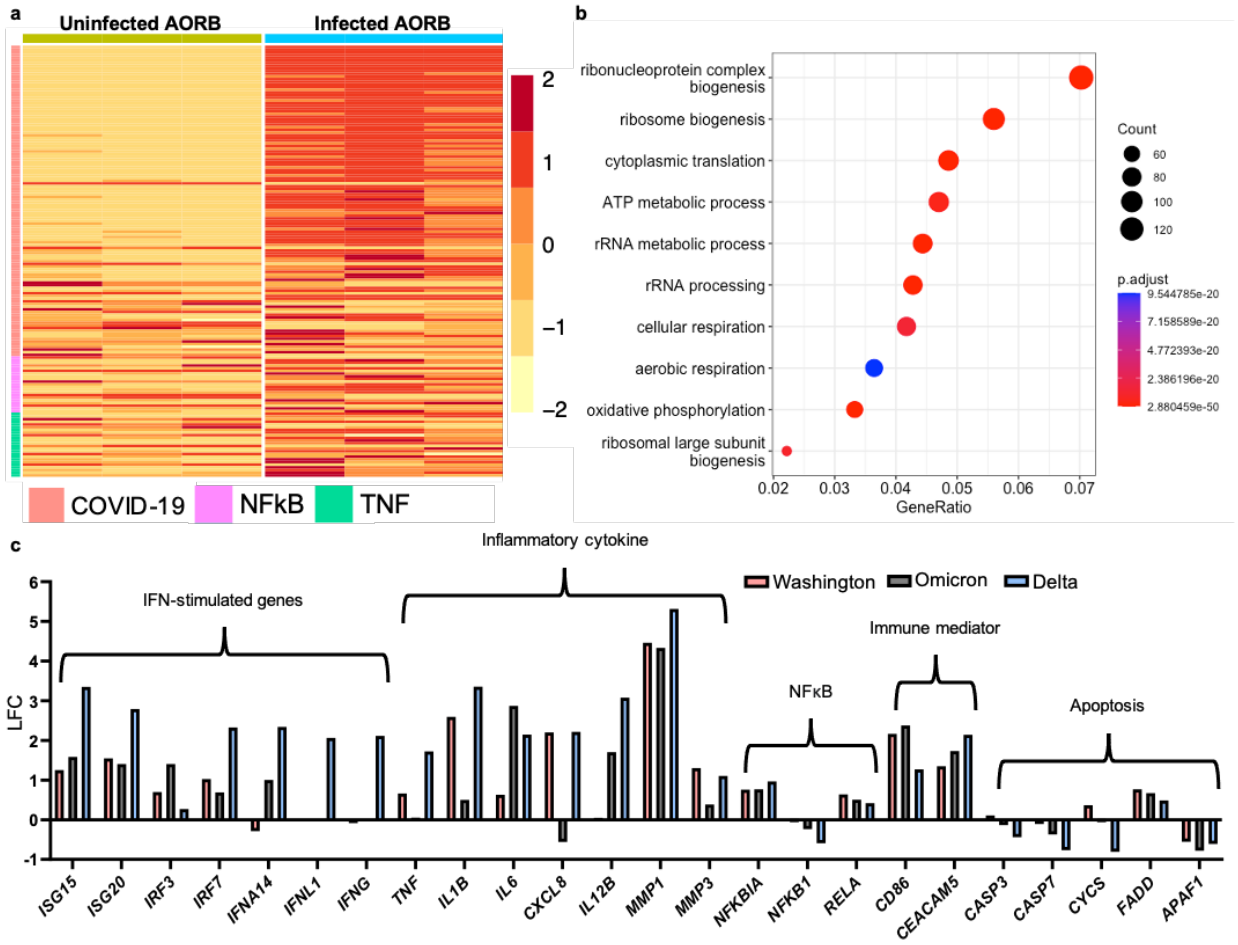

720

721 Fig. 6| **Transcriptomic analysis of infected AORBs. a,** Heatmap summarizing three statistically
722 significant activated pathways comparing infected AORB vs. uninfected control identified by
723 SPIA (COVID-19, hsa05171; NFkB, hsa04064; TNF, hsa04668). **b**, Top 10 statistically significant
724 upregulated biological processes from GO analysis of the enriched gene sets from DGE analysis.
725 **c**, DGE analyses for 5 immune-mediator gene clusters comparing Washington-, Delta-, and
726 Omicron-infected AORBs, respectively, showing different profiles of transcriptomic signatures in
727 AORBs infected by the three strains.

728

729 Table 1| Donor information for hBTECs from Lonza used in this study.

	Age	Sex	Race	Catalog# (Lot#)
Donor #1	29	M	Caucasian	CC-2540S (0000493462)
Donor #2	65	F	Caucasian	CC-2540S (0000619260)
Donor #3	68	M	Caucasian	CC-2540S (0000493462)
Donor #4	21	M	Caucasian	CC-2540S (21TL244297)
Donor #5	73	F	Caucasian	CC-2540S (22TL290876)

730

731

732

733

734 Table 2. Anti-SARS-CoV-2 activities of four tested drugs in conventional 2D cell cultures,
735 Transwell hBTEC-ALI culture, and AORBs.

Compound	2D Immortalized Culture Systems						3D Primary Culture Systems			
	Vero		Caco-2		Calu-3		hBTEC-ALI		AORBs	
	EC_{50} [a] (µM)	EC_{90} [a] (µM)	EC_{50} [a] (µM)	EC_{90} [a] (µM)	EC_{50} [a] (µM)	EC_{90} [a] (µM)	EC_{50} [a] (µM)	EC_{90} [a] (µM)	EC_{50} [a] (µM)	EC_{90} [a] (µM)
Remdesivir	1.8 ± 0.1	2.6 ± 0.2	0.03 ± 0.01	0.08 ± 0.02	0.2 ± 0.1	0.4 ± 0.2	0.4 ± 0.3	0.7 ± 0.5	0.6 ± 1.0	2.3 ± 3.7
AT-511	4.1 - >10	>10	>20	>20	3.9 - >10	>20	0.3 ± 0.3	0.5 ± 0.7	0.8 ± 1.0	1.8 ± 1.1
Nirmatrelvir	2.6 ± 0.6	4.2 ± 0.8	0.08 ± 0.004	0.015 ± 0.01	3.8 ± 1.1	11.1 ± 1.1	0.05 ± 0.003	0.2 ± 0.1	0.7 ± 1.4	1.3 ± 1.0

a EC = 50% (EC50) or 90% (EC90) effective antiviral concentration. All values shown are mean ± standard deviation.

736

737

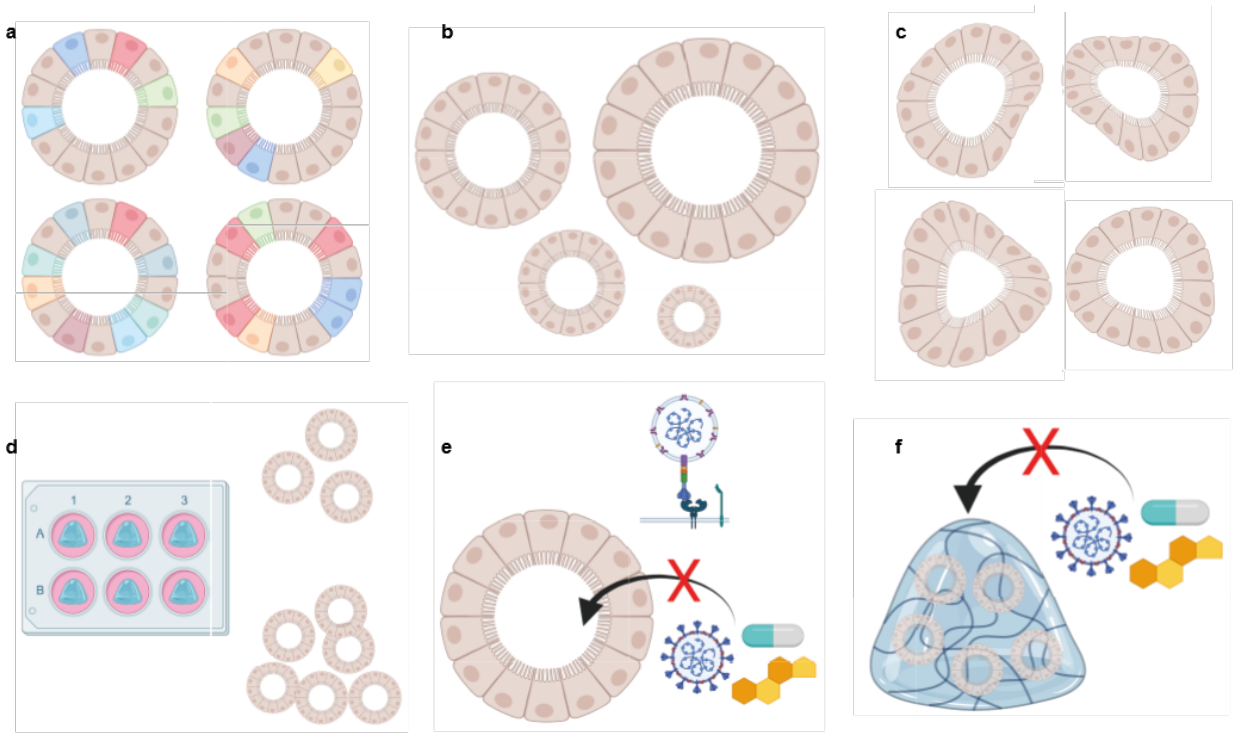

Extended Data Fig. 1| **Limitations of ECM-embedded organoid culture**. **a**, Difficulty controlling cellular heterogeneity of organoids embedded in ECM dome. **b**, High variability in organoid size. **c**, High variability in organoid shape. **d**, Variable numbers of organoids per well. **e**, Apical surface is sequestered away, hence preventing interactions with pathogen or compound of interest. **f**, ECM dome prevents efficient diffusion of pathogen or compound of interest.

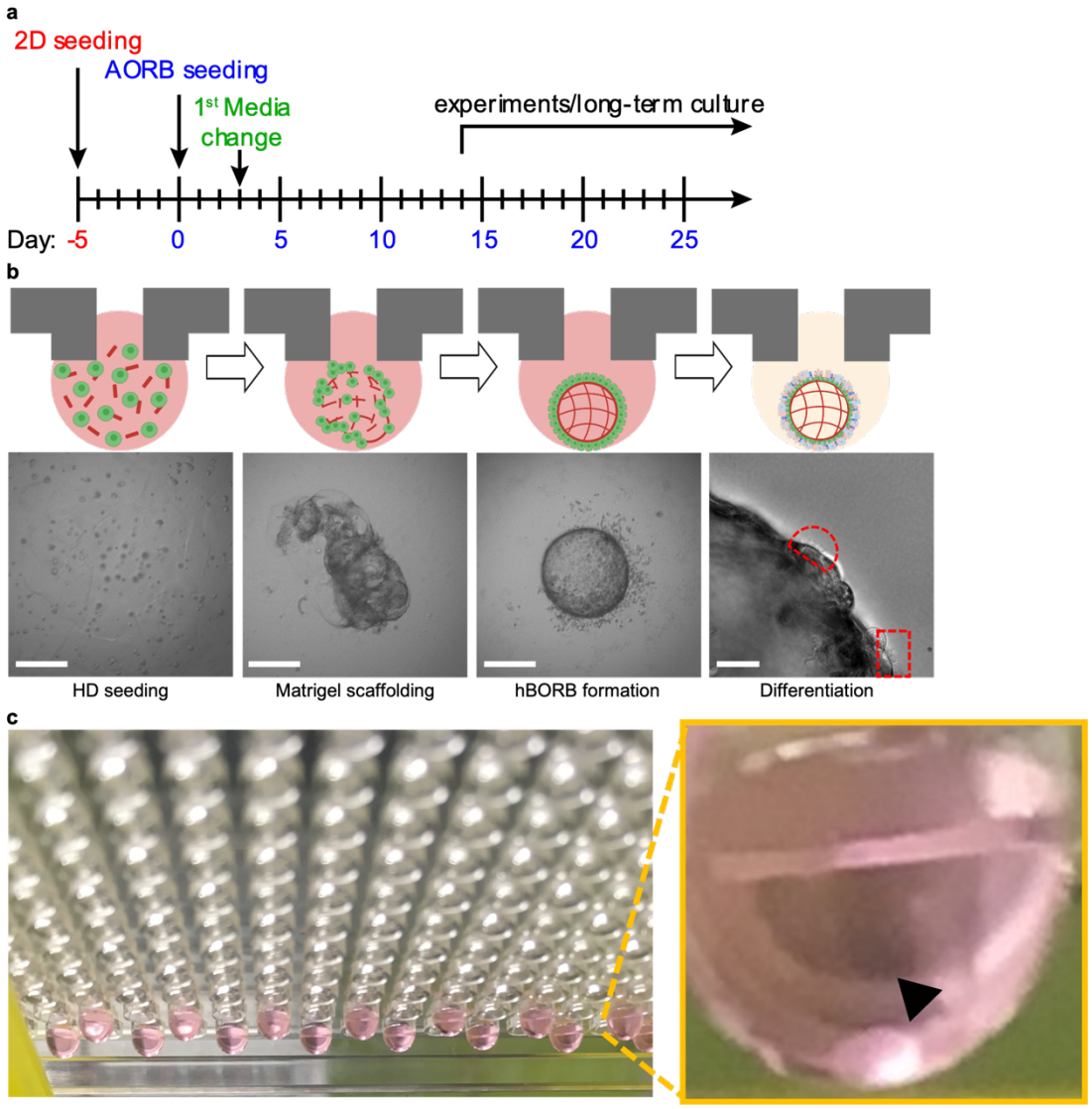

Extended Data Fig. 2| **AORB culture overview**. **a**, Time course summary of AORB culture. **b**, Schematic illustration and representative bright-field images in various phases of AORB culture (left to right, Day 0, 1, 4, 28). **c**, Photo of HD arrays and visual zoom of a singular AORB in one drop. Scale bars, 500 µm and 25 µm for the first three and right-most images, respectively.

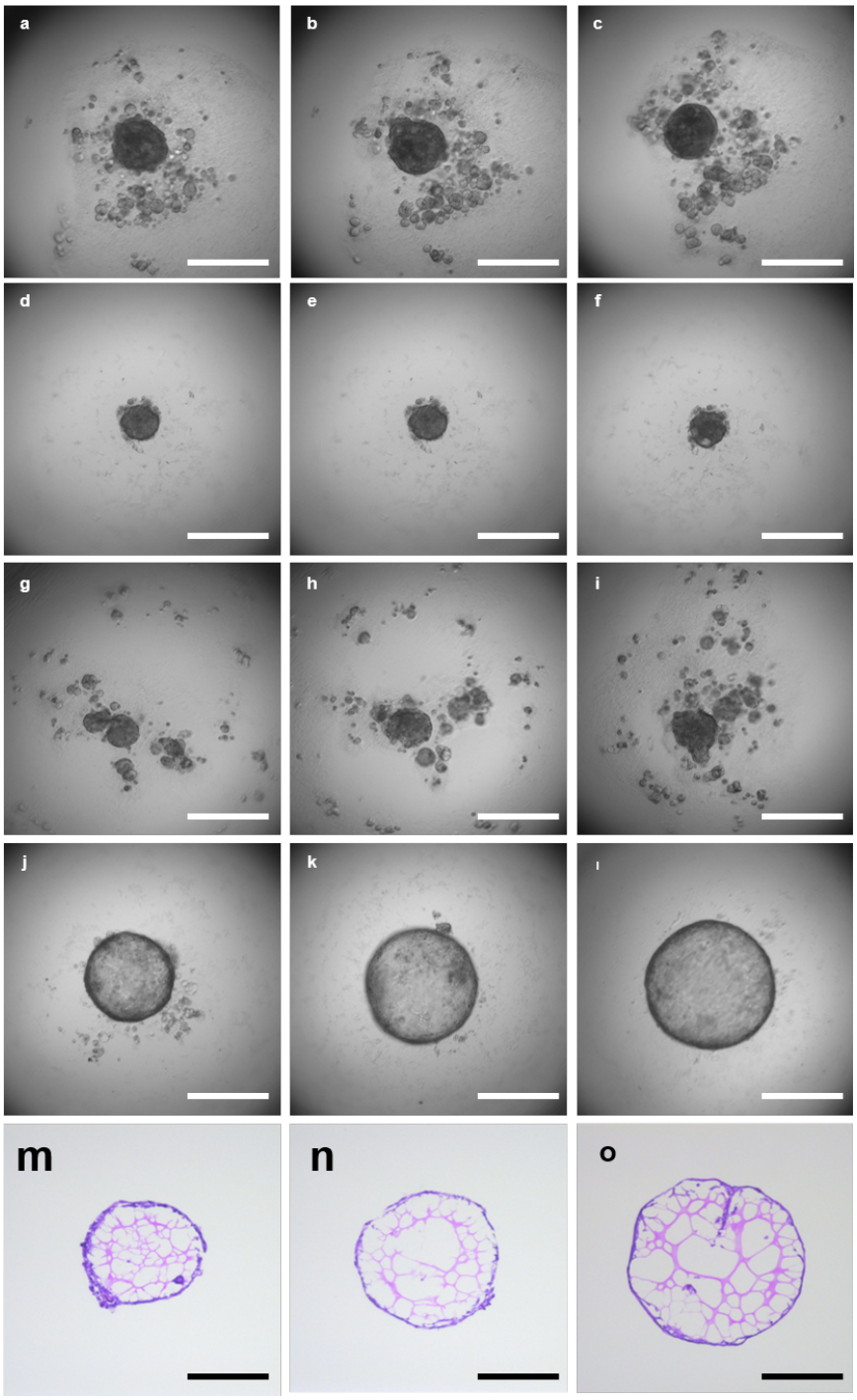

Extended Data Fig. 3| **AORB culture optimization**. **a-c**, 10% FBS+ condition yields multiple spheroid-like structures. **d-f**, Complete serum-free condition yields a singular small spheroid-like structure. **g-i**, Sub-optimal Matrigel also leads to improper formation of organoids. **j-l**, Increasing Matrigel amount within the working range (1300 – 2700 ng per 25 µl drop) augments size of AORBs. **m-o**, H&E staining confirms an acellular hollow core filled with Matrigel and a sheet of epithelial cells around the AORB boundary. Scale bars, 500 µm.

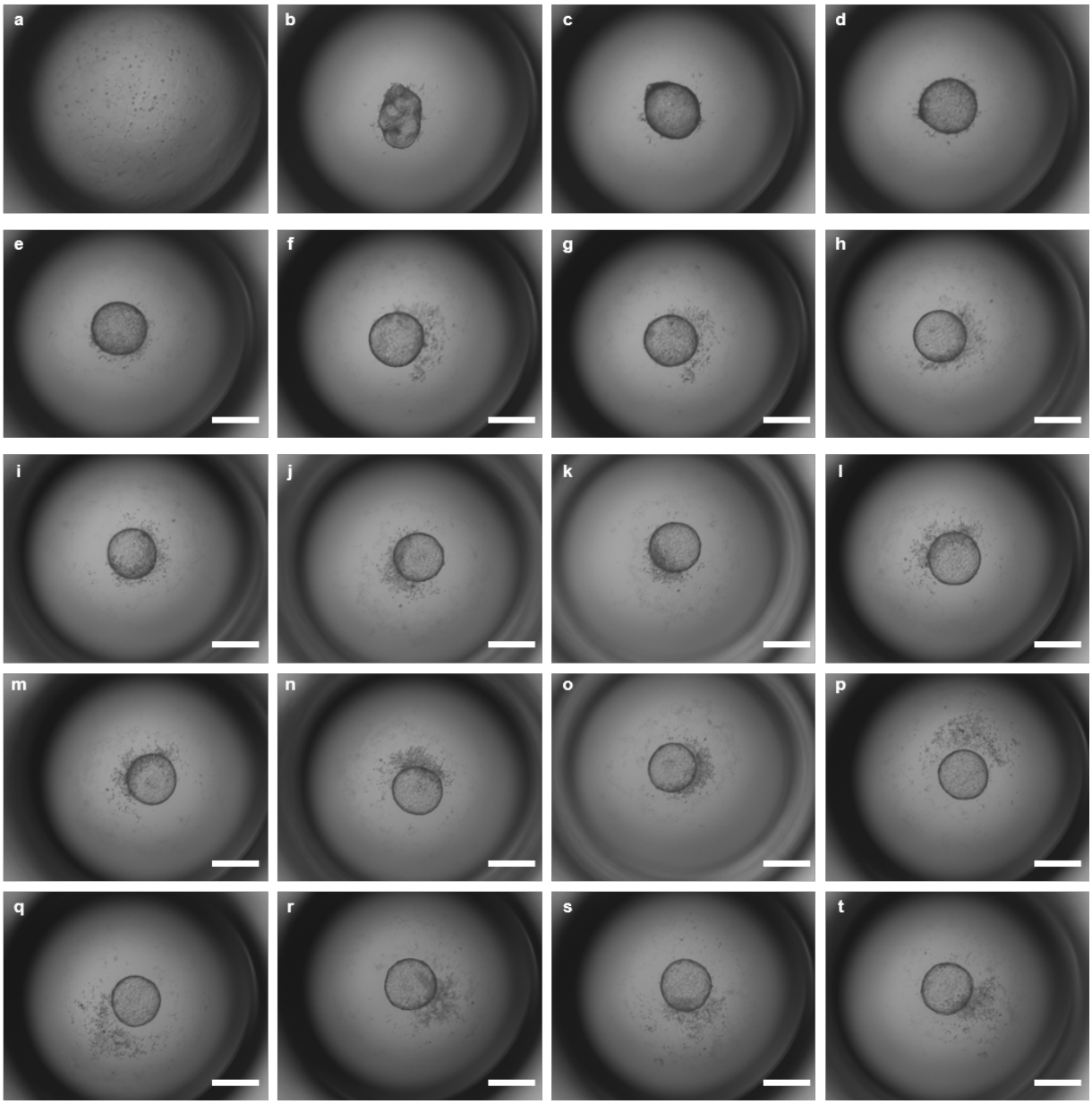

Extended Data Fig. 4| **60-day AORB culture**. **a-t**, Bright-field images of the same AORB at Days 0, 2, 4, 6, 25, 27, 29, 33, 36, 39, 40, 44, 48, 49, 51, 53, 55, 57, 58, and 60. Scale bars, 500 µm.

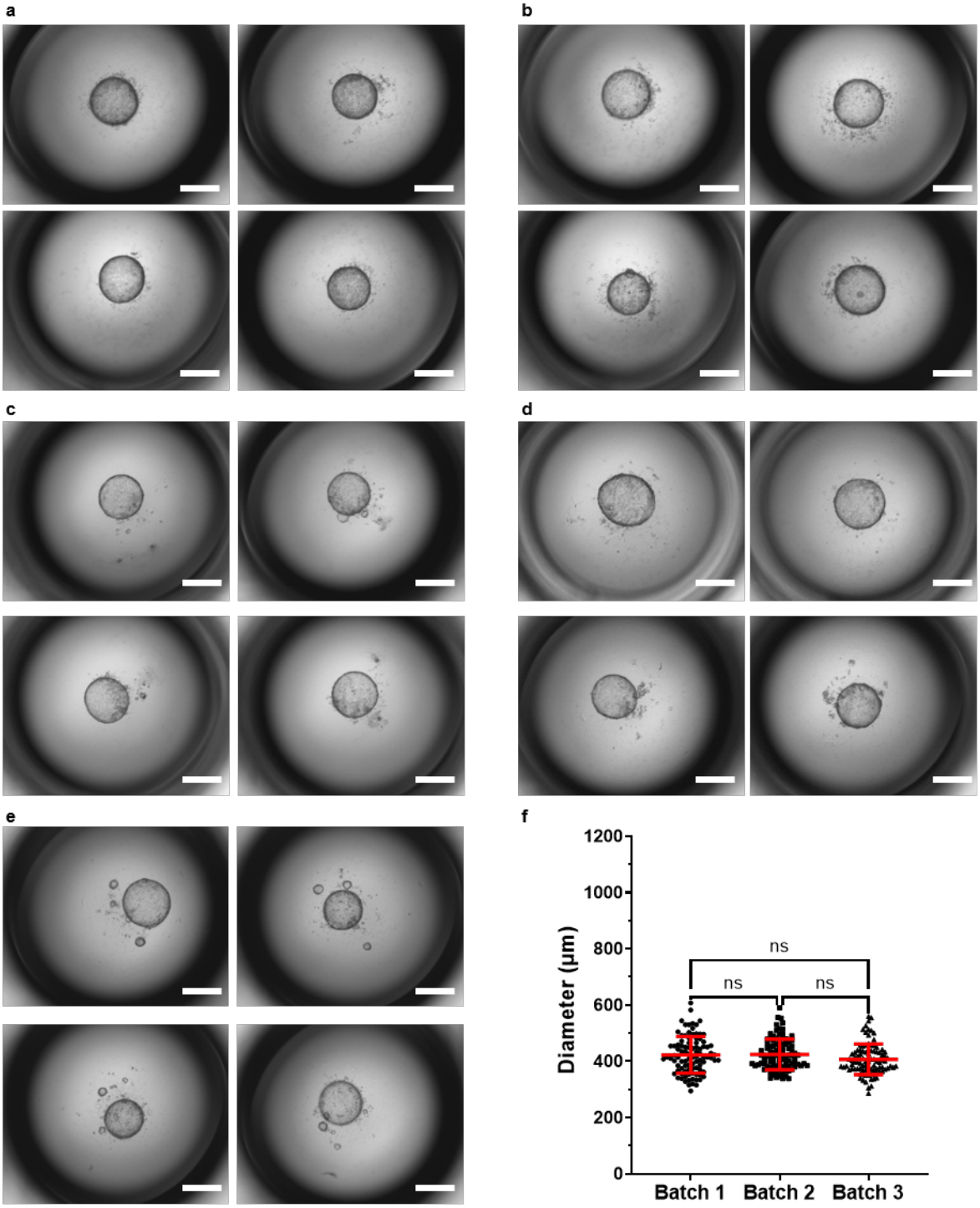

Extended Data Fig. 5| **Biological and technical replicates**. **a-e**, Bright-field images of AORBs derived from 5 different donors with 4 technical replicates each, respectively. **f**, There are no statistical differences in AORB diameter among distinct experimental batches (within donor 1). Scale bars, 500 µm.

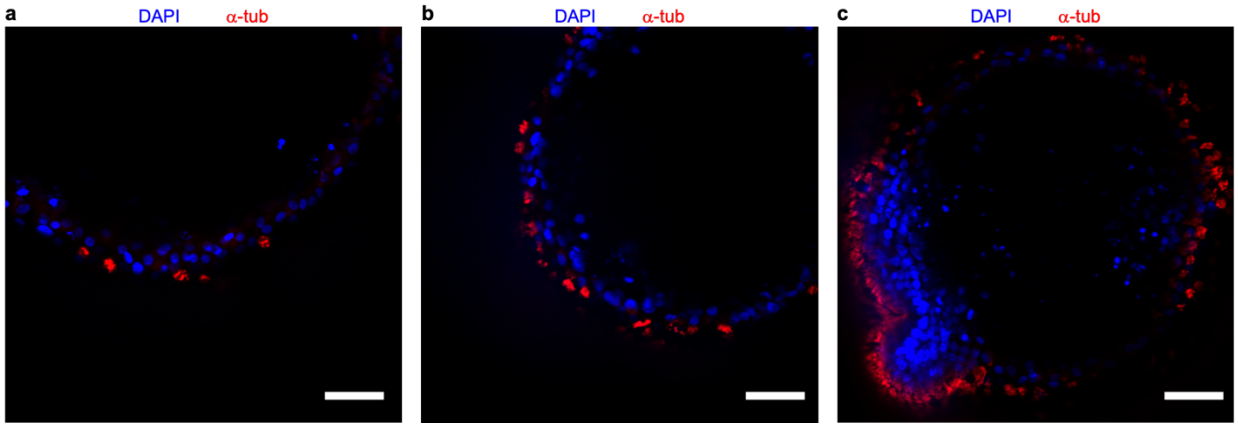

Extended Data Fig. 6| **Time-course** α-tub expression. **a-c**, Increasing fluorescence levels of α-tub AORBs are shown at days 14, 28, and 41, respectively. Scale bars, 100 μm in **a-c.**

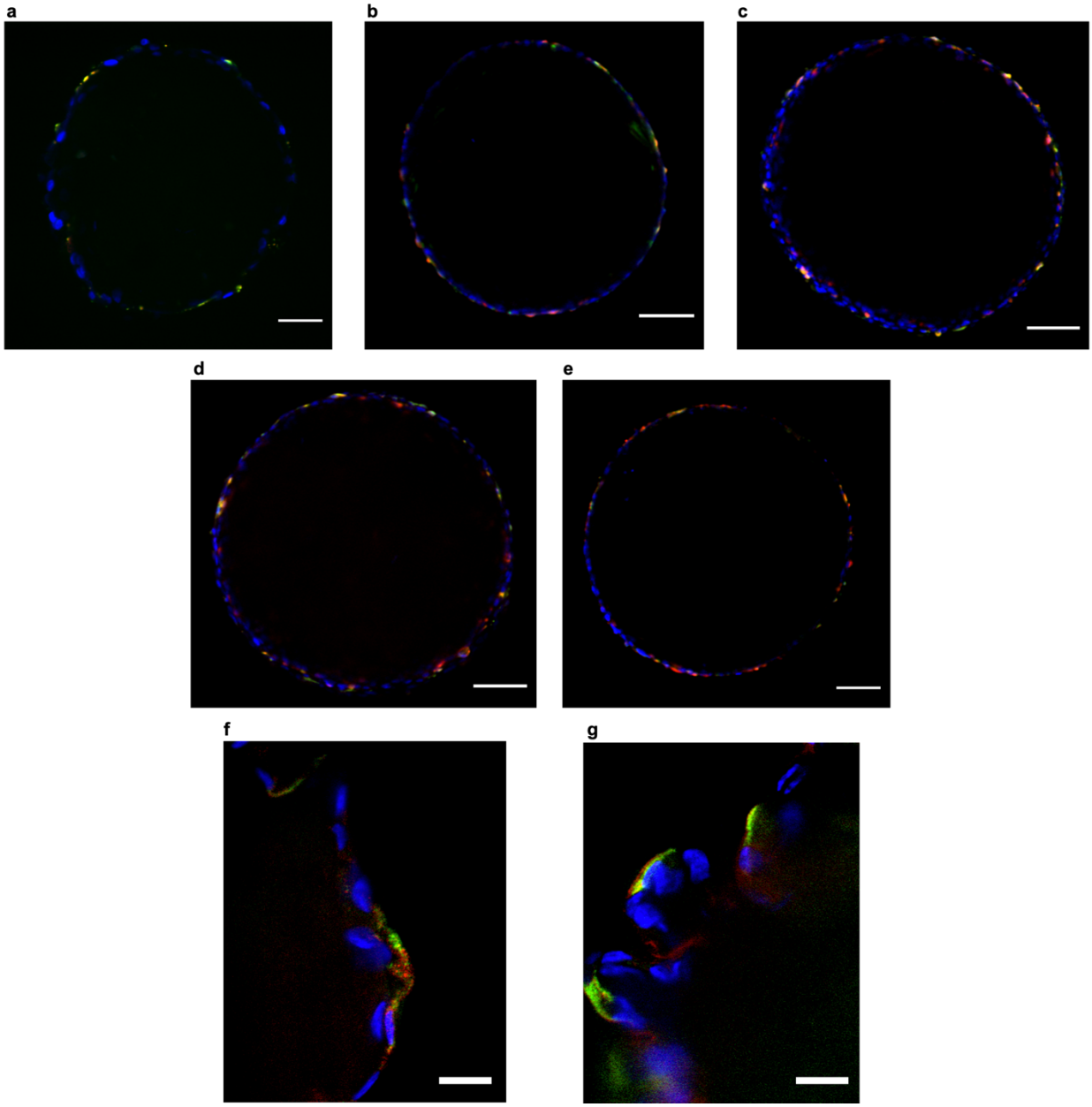

Extended Data Fig. 7| **Additional ACE2/TMPRSS2 Expression Results**. **a-e**, Confocal slices of AORBs stained for ACE2 (green) and TMPRSS2 (red) at days 4, 5, 9, 15, and 30, respectively. TMPRSS2 expression increases more dramatically than ACE2. High magnification images show apical localization of ACE2 (green) and TMPRSS2 (red). Scale bars, 100 µm in **a-e**, and 10 µm in **f-g**.

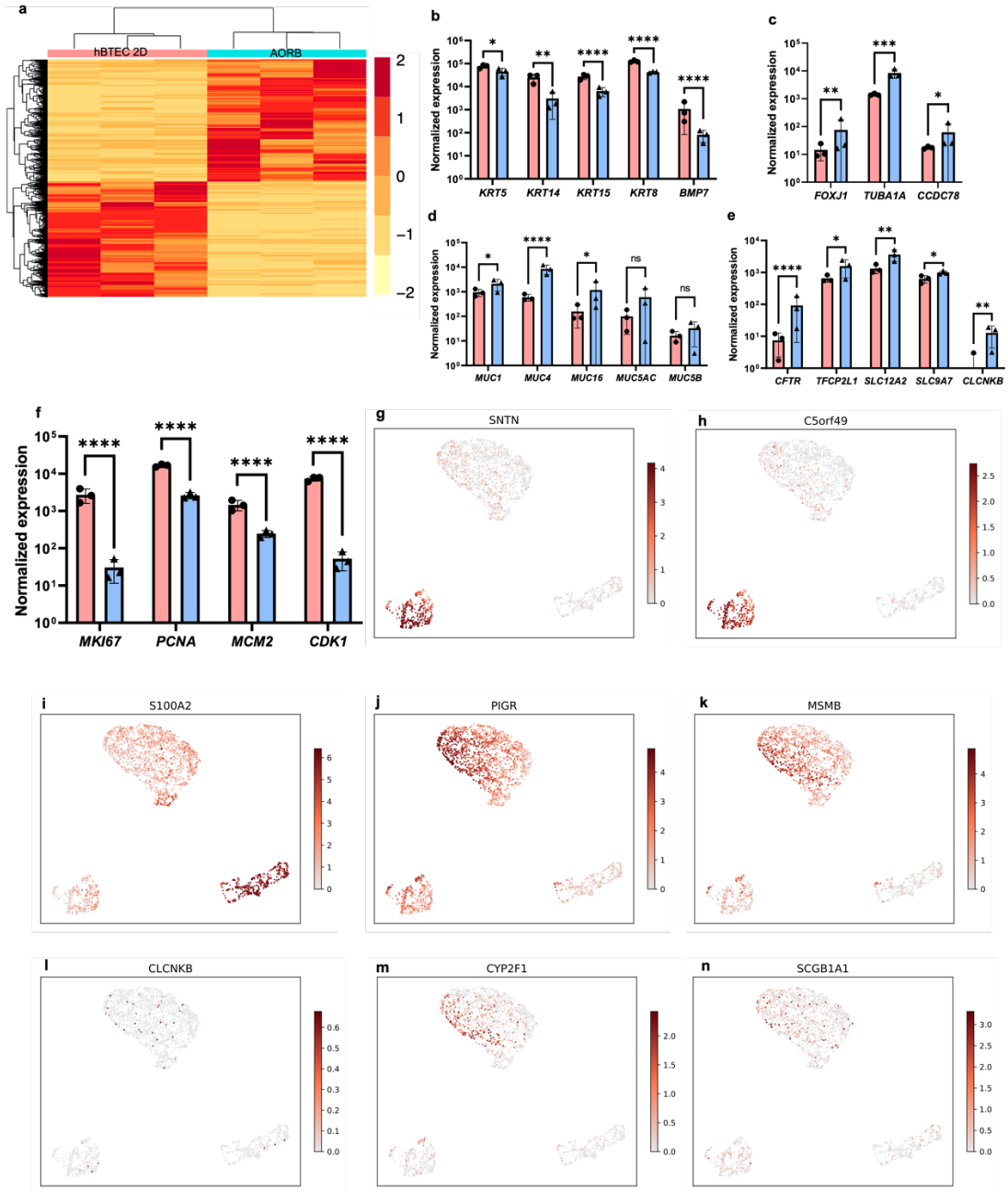

Extended Data Fig. 8| **Extended results from bulkRNAseq analysis**. **a**, Heatmap showing all statistically different genes clustered based on patterns of expression level (pink, 2D monolayer hBTEC culture; cyan, AORBs). **b**, Normalized expression counts for basal cell marker genes decrease in AORBs (blue) relative to their 2D culture counterparts (pink). **c**, Ciliated cell markers were upregulated in AORBs (blue) compared to 2D (pink). **d**, Normalized expression counts for membrane-associated mucins were higher in AORBs (blue) than 2D (pink), whereas canonical goblet cell markers were not statistically different between the two groups. **e**, AORBs exhibit upregulated pulmonary ionocyte markers. **f**, Bulk RNAseq normalized counts for 2D (pink) and AORB (blue) gene markers for proliferation. **g-m**, Expression of marker genes as feature plots on UMAP (**g-h**, ciliated; **i**, basal; **j-k**, goblet; **l-n**, ionocyte).

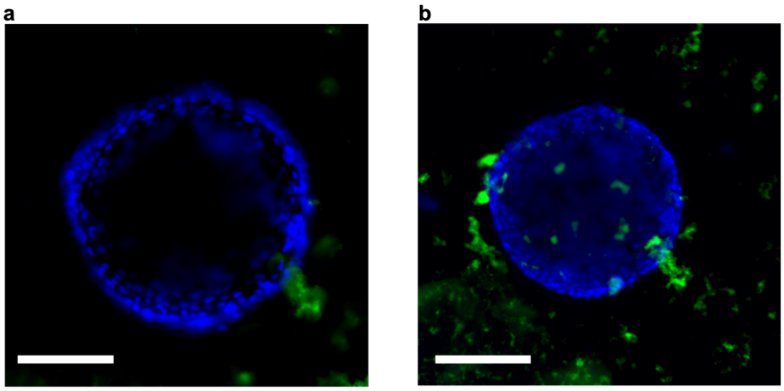

Extended Data Fig. 9| **IL-13-treated AORBs. a-b**, Immunofluorescence images of AORBs counterstained with DAPI (blue) and mucin stained with lectin fluorescent conjugates (green). Scale bars, 250 μm in **a** and **b**.

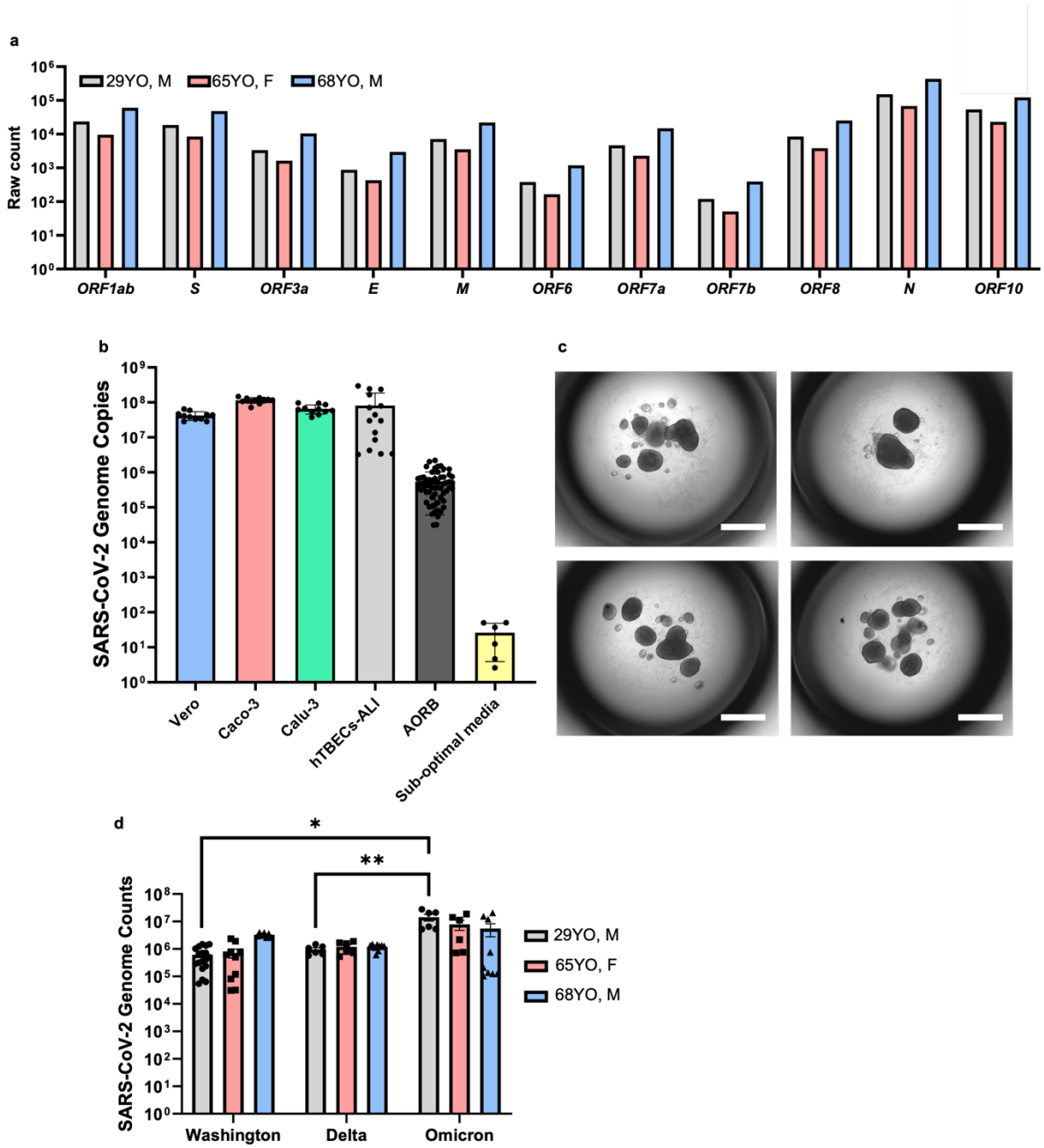

Extended Data Fig. 10| **AORBs are a robust model for SARS-CoV-2 infection studies**. **a**, SARS-CoV-2 genome mappings within Washington-infected AORBs exhibit all viral genes in RNAseq analysis. No viral genes are mapped from uninfected controls. **b**, AORBs show comparable infectibility to other established models. **c**, Sub-optimal media conditions cause improper formation of organoids and do not support viral replication within them. **d**, Omicron variant yields higher infectibility than Delta and Washington across 3 donors. Within variants, there is no statistically significant difference in replication among 3 donors. Scale bars, 500 µm in **c**.

825 Supplementary Table 1| AORB seeding and differentiation media compositions. O and X represent
826 inclusion or exclusion of the component in seeding or differentiation media, respectively.

Media component	Supplier	Catalogue number	Final concentration	Seeding	Differentiation
Cells	-	-	120,000 cells/mL	O	X
Methylcellulose	Sigma-Aldrich	94378	0.24%	O	X
Matrigel	Corning	356231	50-100 µg/mL	O	X
Hydrocortisone	Sigma-Aldrich	07925	1x	X	O
DAPT	Tocris	2634	2 µM	X	O
PneumaCult™ Airway Organoid Seeding Supplement	STEMCELL Technologies	05062	10%	O	X
PneumaCult™ Airway Organoid Basal Medium	STEMCELL Technologies	05061	1x	O	O
PneumaCult™ Airway Organoid Differentiation Supplement	STEMCELL Technologies	05063	10%	X	O

827

828

829

830 Supplementary Table 2| Total level of active nucleoside triphosphate (AT-9010).

	Vero[a]	Caco-2[a]	Calu-3[a]	hBTEC-ALI[a]
AT-9010 (pmol/10^6 cells)	0.89 ± 0.05	30.1 ± 2.41	4.93 ± 0.06	170.8 ± 62.51

[a]Cells were treated with 10 µM of AT-511 for 4 h at 37°C.

831

832

833

834

835

836

837

838

839 Supplementary Table 3. Antiviral response by the three donors. The overall variability attributes
840 to the female donor, with more consistent results from other two male donors.

	68YO, M		**65YO, F**		**29YO, M**	
	EC_{50}[a] (μM)	**EC_{90}[a] (μM)**	**EC_{50}[a] (μM)**	**EC_{90}[a] (μM)**	**EC_{50}[a] (μM)**	**EC_{90}[a] (μM)**
Remdesivir	0.3 ± 0.2	1.3 ± 0.9	1.8 ± 2.3	7.3 ± 8.3	0.4 ± 0.08	1.1 ± 0.7
AT-511	1.1 ± 1.5	2.5 ± 0.9	0.8 ± 0.9	2.3 ± 1.1	0.3 ± 0.03	1.2 ± 0.04
Nirmatrelvir	0.08 ± 0.07	1.0 ± 0.8	0.1	1.0	0.3 ± 0.1	1.7 ± 1.4

a EC = 50% (EC50) or 90% (EC90) effective antiviral concentration.

841

842 **References**

843 1. Boj, S. F. *et al.* Forskolin-induced swelling in intestinal organoids: an in vitro assay for
844 assessing drug response in cystic fibrosis patients. *J. Vis. Exp. JoVE* (2017)
845 doi:https://doi.org/10.3791/55159.
846 2. Zhang, L., Peeples, M. E., Boucher, R. C., Collins, P. L. & Pickles, R. J. Respiratory
847 syncytial virus infection of human airway epithelial cells is polarized, specific to ciliated
848 cells, and without obvious cytopathology. *J. Virol.* **76**, 5654–5666 (2002).
849 3. Hughey, P. G., Compans, R. W., Zebedee, S. L. & Lamb, R. A. Expression of the influenza
850 A virus M2 protein is restricted to apical surfaces of polarized epithelial cells. *J. Virol.* **66**,
851 5542–5552 (1992).
852 4. Vanderheiden, A. *et al.* Type I and Type III Interferons Restrict SARS-CoV-2 Infection of
853 Human Airway Epithelial Cultures. *J. Virol.* **94**, e00985-20 (2020).
854 5. Hao, S. *et al.* Long-term modeling of SARS-CoV-2 infection of in vitro cultured polarized
855 human airway epithelium. *mBio* **11**, 10.1128/mbio.02852-20 (2020).
856 6. Kim, J., Koo, B.-K. & Knoblich, J. A. Human organoids: model systems for human biology
857 and medicine. *Nat. Rev. Mol. Cell Biol.* **21**, 571–584 (2020).
858 7. Parigoris, E. *et al.* Cancer cell invasion of mammary organoids with basal-in phenotype. *Adv.*
859 *Healthc. Mater.* **10**, 2000810 (2021).
860 8. Lee, S. *et al.* High-throughput formation and image-based analysis of basal-in mammary
861 organoids in 384-well plates. *Sci. Rep.* **12**, 317 (2022).
862 9. Parigoris, E., Lee, J.-H., Liu, A. Y., Zhao, X. & Takayama, S. Extended longevity
863 geometrically-inverted proximal tubule organoids. *Biomaterials* **290**, 121828 (2022).
864 10. Mertz, D. R. *et al.* Triple-negative breast cancer cells invade adipocyte/preadipocyte-
865 encapsulating geometrically inverted mammary organoids. *Integr. Biol.* **15**, zyad004 (2023).

866 11. Salahudeen, A. A. *et al.* Progenitor identification and SARS-CoV-2 infection in human distal
867 lung organoids. *Nat. 2020 5887839* **588**, 670–675 (2020).
868 12. Chiu, M. C. *et al.* Apical-out human airway organoids modeling SARS-CoV-2 infection.
869 *Viruses* **15**, 1166 (2023).
870 13. Han, Y., Yang, L., Lacko, L. A. & Chen, S. Human organoid models to study SARS-CoV-2
871 infection. *Nat. Methods* **19**, 418–428 (2022).
872 14. SUNRISE-3: efficacy and safety of bemnifosbuvir in high-risk outpatients with COVID-19
873 [online]. Available at https://clinicaltrials.gov/ct2/show/NCT05629962 (2023).
874 15. Tung, Y.-C. *et al.* High-throughput 3D spheroid culture and drug testing using a 384 hanging
875 drop array. *Analyst* **136**, 473–478 (2011).
876 16. Barkauskas, C. E. *et al.* Lung organoids: current uses and future promise. *Development* **144**,
877 986–997 (2017).
878 17. Gras, D. *et al.* Epithelial ciliated beating cells essential for ex vivo ALI culture growth. *BMC*
879 *Pulm. Med.* **17**, 80 (2017).
880 18. Plasschaert, L. W. *et al.* A single-cell atlas of the airway epithelium reveals the CFTR-rich
881 pulmonary ionocyte. *Nature* **560**, 377–381 (2018).
882 19. Travaglini, K. J. *et al.* A molecular cell atlas of the human lung from single-cell RNA
883 sequencing. *Nature* **587**, 619–625 (2020).
884 20. Hayashi, Y. *et al.* Downregulation of rRNA transcription triggers cell differentiation. *PLOS*
885 *ONE* **9**, e98586 (2014).
886 21. Sikkema, L. *et al.* An integrated cell atlas of the lung in health and disease. *Nat. Med.* **29**,
887 1563–1577 (2023).

888 22. Mercer, R. R., Russell, M. L., Roggli, V. L. & Crapo, J. D. Cell number and distribution in
889 human and rat airways. *Am. J. Respir. Cell Mol. Biol.* **10**, 613–624 (1994).
890 23. Fahy, J. V. Goblet cell and mucin gene abnormalities in asthma. *Chest* **122**, 320S-326S
891 (2002).
892 24. Kondo, M., Tamaoki, J., Takeyama, K., Nakata, J. & Nagai, A. Interleukin-13 induces goblet
893 cell differentiation in primary cell culture from guinea pig tracheal epithelium. *Am. J. Respir.*
894 *Cell Mol. Biol.* **27**, 536–541 (2002).
895 25. Laoukili, J. *et al.* IL-13 alters mucociliary differentiation and ciliary beating of human
896 respiratory epithelial cells. *J. Clin. Invest.* **108**, 1817–1824 (2001).
897 26. Seibold, M. A. Interleukin-13 stimulation reveals the cellular and functional plasticity of the
898 airway epithelium. *Ann. Am. Thorac. Soc.* **15**, S98–S102 (2018).
899 27. Jia, H. P. *et al.* ACE2 receptor expression and severe acute respiratory syndrome coronavirus
900 infection depend on differentiation of human airway epithelia. *J. Virol.* **79**, 14614–14621
901 (2005).
902 28. Sims, A. C. *et al.* Severe acute respiratory syndrome coronavirus infection of human ciliated
903 airway epithelia: role of ciliated cells in viral spread in the conducting airways of the lungs.
904 *J. Virol.* **79**, 15511–15524 (2005).
905 29. Ren, X. *et al.* Analysis of ACE2 in polarized epithelial cells: surface expression and function
906 as receptor for severe acute respiratory syndrome-associated coronavirus. *J. Gen. Virol.* **87**,
907 1691–1695 (2006).
908 30. Lee, I. T. *et al.* ACE2 localizes to the respiratory cilia and is not increased by ACE inhibitors
909 or ARBs. *Nat. Commun.* **11**, 5453 (2020).

910 31. Bertram, S. *et al.* Influenza and SARS-coronavirus activating proteases TMPRSS2 and HAT
911 are expressed at multiple sites in human respiratory and gastrointestinal tracts. *PLOS ONE* **7**,
912 e35876 (2012).
913 32. Sungnak, W. *et al.* SARS-CoV-2 entry factors are highly expressed in nasal epithelial cells
914 together with innate immune genes. *Nat. Med.* **26**, 681–687 (2020).
915 33. Xie, X. *et al.* An infectious cDNA clone of SARS-CoV-2. *Cell Host Microbe* **27**, 841-848.e3
916 (2020).
917 34. Hui, K. P. Y. *et al.* SARS-CoV-2 Omicron variant replication in human bronchus and lung
918 ex vivo. *Nature* **603**, 715–720 (2022).
919 35. Eastman, R. T. *et al.* Remdesivir: a review of its discovery and development leading to
920 emergency use authorization for treatment of COVID-19. *ACS Cent. Sci.* **6**, 672–683 (2020).
921 36. Jayk Bernal, A. *et al.* Molnupiravir for oral treatment of Covid-19 in nonhospitalized
922 patients. *N. Engl. J. Med.* **386**, 509–520 (2022).
923 37. Tao, S. *et al.* Comparison of anti-SARS-CoV-2 activity and intracellular metabolism of
924 remdesivir and its parent nucleoside. *Curr. Res. Pharmacol. Drug Discov.* **2**, 100045 (2021).
925 38. Pruijssers, A. J. *et al.* Remdesivir inhibits SARS-CoV-2 in human lung cells and chimeric
926 SARS-CoV expressing the SARS-CoV-2 RNA polymerase in mice. *Cell Rep.* **32**, 107940
927 (2020).
928 39. Wang, M. *et al.* Remdesivir and chloroquine effectively inhibit the recently emerged novel
929 coronavirus (2019-nCoV) in vitro. *Cell Res.* **30**, 269–271 (2020).
930 40. Choy, K.-T. *et al.* Remdesivir, lopinavir, emetine, and homoharringtonine inhibit SARS-
931 CoV-2 replication in vitro. *Antiviral Res.* **178**, 104786 (2020).

932 41. Good, S. S. *et al.* AT-527, a double prodrug of a guanosine nucleotide analog, is a potent
933 inhibitor of SARS-CoV-2 in vitro and a promising oral antiviral for treatment of COVID-19.
934 *Antimicrob. Agents Chemother.* **65**, 10.1128/aac.02479-20 (2021).
935 42. Do, T. N. D. *et al.* A robust SARS-CoV-2 replication model in primary human epithelial
936 cells at the air liquid interface to assess antiviral agents. *Antiviral Res.* **192**, 105122 (2021).
937 43. Bigorgne, A. E. *et al.* TTC7A mutations disrupt intestinal epithelial apicobasal polarity. *J.*
938 *Clin. Invest.* **124**, 328–337 (2014).
939 44. Mahase, E. Covid-19: Pfizer's paxlovid is 89% effective in patients at risk of serious illness,
940 company reports. *BMJ* **375**, n2713 (2021).
941 45. Pedersen, P. S., Frederiksen, O., Holstein-Rathlou, N.-H., Larsen, P. L. & Qvortrup, K. Ion
942 transport in epithelial spheroids derived from human airway cells. *Am. J. Physiol.-Lung Cell.*
943 *Mol. Physiol.* **276**, L75–L80 (1999).
944 46. Pedersen, P. S., Holstein-Rathlou, N.-H., Larsen, P. L., Qvortrup, K. & Frederiksen, O. Fluid
945 absorption related to ion transport in human airway epithelial spheroids. *Am. J. Physiol.-*
946 *Lung Cell. Mol. Physiol.* **277**, L1096–L1103 (1999).
947 47. Akhtar, N. & Streuli, C. H. An integrin–ILK–microtubule network orients cell polarity and
948 lumen formation in glandular epithelium. *Nat. Cell Biol.* **15**, 17–27 (2013).
949 48. Liu, B. *et al.* Overexpression of β1 integrin contributes to polarity reversal and a poor
950 prognosis of breast invasive micropapillary carcinoma. *Oncotarget* **9**, 4338–4353 (2017).
951 49. Wang, A. Z., Ojakian, G. K. & Nelson, W. J. Steps in the morphogenesis of a polarized
952 epithelium. II. Disassembly and assembly of plasma membrane domains during reversal of
953 epithelial cell polarity in multicellular epithelial (MDCK) cysts. *J. Cell Sci.* **95**, 153–165
954 (1990).

955 50. Wilson, P. D. Apico-basal polarity in polycystic kidney disease epithelia. *Biochim. Biophys.*
956 *Acta BBA - Mol. Basis Dis.* **1812**, 1239–1248 (2011).
957 51. O'Brien, L. E. *et al.* Rac1 orientates epithelial apical polarity through effects on basolateral
958 laminin assembly. *Nat. Cell Biol.* **3**, 831–838 (2001).
959 52. Zhou, J. *et al.* Differentiated human airway organoids to assess infectivity of emerging
960 influenza virus. *Proc. Natl. Acad. Sci.* **115**, 6822–6827 (2018).
961 53. Okuyama, H. *et al.* Dynamic change of polarity in primary cultured spheroids of human
962 colorectal adenocarcinoma and its role in metastasis. *Am. J. Pathol.* **186**, 899–911 (2016).
963 54. Co, J. Y. *et al.* Controlling epithelial polarity: a human enteroid model for host-pathogen
964 interactions. *Cell Rep.* **26**, 2509-2520.e4 (2019).
965 55. Stroulios, G. *et al.* Apical-out airway organoids as a platform for studying viral infections
966 and screening for antiviral drugs. *Sci. Rep.* **12**, 7673 (2022).
967 56. Stroulios, G. *et al.* Culture methods to study apical-specific interactions using intestinal
968 organoid models. *JoVE J. Vis. Exp.* **2021**, e62330 (2021).
969 57. Wijesekara, P. *et al.* Engineering rotating apical-out airway organoid for assessing
970 respiratory cilia motility. *bioRxiv* 2022.01.15.476455 (2022)
971 doi:10.1101/2022.01.15.476455.
972 58. Yang, M. *et al.* Inhibition of mitochondrial function by metformin increases glucose uptake,
973 glycolysis and GDF-15 release from intestinal cells. *Sci. Rep. 2021 111* **11**, 1–20 (2021).
974 59. Nash, T. J., Morris, K. M., Mabbott, N. A. & Vervelde, L. Inside-out chicken enteroids with
975 leukocyte component as a model to study host–pathogen interactions. *Commun. Biol. 2021*
976 *41* **4**, 1–15 (2021).

977 60. Li, Y. *et al.* Next-generation porcine intestinal organoids: an apical-out organoid model for
978 swine enteric virus infection and immune response investigations. *J. Virol.* **94**, (2020).
979 61. Ramis, G. *et al.* Porcine intestinal apical-out organoid model for gut function study. *Anim.*
980 *2022 Vol 12 Page 372* **12**, 372 (2022).
981 62. Smith, D. *et al.* The development of ovine gastric and intestinal organoids for studying
982 ruminant host-pathogen interactions. *Front. Cell. Infect. Microbiol.* **11**, 821 (2021).
983 63. Co, J. Y., Margalef-Català, M., Monack, D. M. & Amieva, M. R. Controlling the polarity of
984 human gastrointestinal organoids to investigate epithelial biology and infectious diseases.
985 *Nat. Protoc. 2021 1611* **16**, 5171–5192 (2021).
986 64. Boecking, C. A. *et al.* A simple method to generate human airway epithelial organoids with
987 externally orientated apical membranes. *Am. J. Physiol.-Lung Cell. Mol. Physiol.* **322**, L420–
988 L437 (2022).
989 65. Gumuskaya, G. *et al.* Motile living biobots self-construct from adult human somatic
990 progenitor seed cells. *Adv. Sci.* **n/a**, 2303575.
991 66. Kassis, T., Hernandez-Gordillo, V., Langer, R. & Griffith, L. G. OrgaQuant: Human
992 Intestinal Organoid Localization and Quantification Using Deep Convolutional Neural
993 Networks. *Sci. Rep.* **9**, 12479 (2019).
994 67. Zhu, N. *et al.* Morphogenesis and cytopathic effect of SARS-CoV-2 infection in human
995 airway epithelial cells. *Nat. Commun.* **11**, 3910 (2020).
996 68. Fiege, J. K. *et al.* Single cell resolution of SARS-CoV-2 tropism, antiviral responses, and
997 susceptibility to therapies in primary human airway epithelium. *PLOS Pathog.* **17**, e1009292
998 (2021).

999 69. Bridges, J. P., Vladar, E. K., Huang, H. & Mason, R. J. Respiratory epithelial cell responses
1000 to SARS-CoV-2 in COVID-19. *Thorax* **77**, 203–209 (2022).
1001 70. Shalamova, L. *et al.* Omicron variant of SARS-CoV-2 exhibits an increased resilience to the
1002 antiviral type I interferon response. *PNAS Nexus* **1**, pgac067 (2022).
1003 71. Nchioua, R. *et al.* Reduced replication but increased interferon resistance of SARS-CoV-2
1004 Omicron BA.1. *Life Sci. Alliance* **6**, e202201745 (2023).
1005 72. Pirzada, R. H., Haseeb, M., Batool, M., Kim, M. & Choi, S. Remdesivir and ledipasvir
1006 among the FDA-approved antiviral drugs have potential to inhibit SARS-CoV-2 replication.
1007 *Cells* **10**, 1052 (2021).
1008 73. Li, R. *et al.* Key metabolic enzymes involved in remdesivir activation in human lung cells.
1009 *Antimicrob. Agents Chemother.* **65**, 10.1128/aac.00602-21 (2021).
1010 74. Liu, Y., Sun, S., Li, J., Wang, W. & Zhu, H.-J. Cell-dependent activation of ProTide
1011 prodrugs and its implications in antiviral studies. *ACS Pharmacol. Transl. Sci.* **6**, 1340–1346
1012 (2023).
1013 75. Imai, T. & Ohura, K. The role of intestinal carboxylesterase in the oral absorption of
1014 prodrugs. *Curr. Drug Metab.* **11**, 793–805.
1015 76. Atea Pharmaceuticals. COVID-19 and Bemnifosbuvir: In Vitro Results Against COVID-19
1016 Variants. Retrieved from https://ateapharma.com/covid-19/bemnifosbuvir/.
1017 77. Pfizer. Paxlovid Annex 1. Chp 5, Section 5.1: Pharmacodynamic properties. [Online].
1018 Available at https://www.ema.europa.eu/en/documents/product-information/paxlovid-epar-
1019 product-information_en.pdf.
1020 78. *S.5002 - 117th Congress (2021-2022): FDA Modernization Act 2.0. (2022, September 29).*
1021 *Available at https://www.congress.gov/bill/117th-congress/senate-bill/5002*.

1022 79. Siegel, D. *et al.* Discovery and synthesis of a phosphoramidate prodrug of a pyrrolo[2,1-
1023 f][triazin-4-amino] adenine C-nucleoside (GS-5734) for the treatment of ebola and emerging
1024 viruses. *J. Med. Chem.* **60**, 1648–1661 (2017).
1025 80. Sommadossi, J.-P. & Moussa, A. Beta-D-2'-deoxy-2'-alpha-fluoro-2'-beta-C-substituted-2-
1026 modified-N6-substituted purine nucleotides for HCV treatment. Patent. US20160257706A1.
1027 (2016).
1028 81. Owen, D. R. *et al.* Nitrile-containing antiviral compounds. Patent. WO2021250648A1.
1029 (2021).
1030 82. Dekkers, J. F. *et al.* High-resolution 3D imaging of fixed and cleared organoids. *Nat. Protoc.*
1031 **14**, 1756–1771 (2019).
1032 83. Andrew, S. FastQC: A Quality Control Tool for High Throughput Sequence Data. [Online].
1033 Available at https://www.bioinformatics.babraham.ac.uk/projects/fastqc/.
1034 84. Bolger, A. M., Lohse, M. & Usadel, B. Trimmomatic: a flexible trimmer for Illumina
1035 sequence data. *Bioinformatics* **30**, 2114–2120 (2014).
1036 85. Dobin, A. *et al.* STAR: ultrafast universal RNA-seq aligner. *Bioinformatics* **29**, 15–21
1037 (2013).
1038 86. Love, M. I., Huber, W. & Anders, S. Moderated estimation of fold change and dispersion for
1039 RNA-seq data with DESeq2. *Genome Biol.* **15**, 550 (2014).
1040 87. Stephens, M. False discovery rates: a new deal. *Biostatistics* **18**, 275–294 (2017).
1041 88. Yu, G., Wang, L.-G., Han, Y. & He, Q.-Y. clusterProfiler: an R package for comparing
1042 biological themes among gene clusters. *OMICS J. Integr. Biol.* **16**, 284–287 (2012).
1043 89. Tarca, A. L. *et al.* A novel signaling pathway impact analysis. *Bioinformatics* **25**, 75–82
1044 (2009).

1045 90. Clark, I. C. *et al.* Microfluidics-free single-cell genomics with templated emulsification. *Nat.*
1046 *Biotechnol.* **41**, 1557–1566 (2023).
1047